A Molecular Dynamics Study of the Elastic Properties of Cu-Zr-Al Metallic Glasses

Luka Kemme

4th March 2025

Abstract

This thesis investigates the elastic properties of Cu-Zr-Al metallic glasses using molecular dynamics simulations. Metallic glasses, known for their amorphous atomic structure, often exhibit superior mechanical properties compared to their crystalline counterparts. By leveraging rapid cooling techniques, these materials avoid crystallization, transitioning into a glassy phase with enhanced hardness and strength.

Through molecular dynamics simulations, the study models the melt-quench process to generate Cu-Zr-Al metallic glass structures and compares their mechanical properties with those of corresponding crystalline phases. The elastic stiffness tensor is computed using both direct deformation and stress fluctuation methods, allowing for the determination of bulk, shear, and Young's moduli. These values are then used to estimate material hardness based on empirical relationships.

The findings highlight notable increases in hardness for specific alloy compositions when transitioning from a crystalline to an amorphous state. Additionally, the results underscore the effectiveness of computational methods in predicting the mechanical properties of metallic glasses, offering a viable alternative to experimental approaches. This research contributes to the broader understanding of glass-forming alloys and their potential applications in designing advanced materials with superior mechanical performance.

Contents

1 Introduction

1.1 Hard Metals

Hard materials are ubiquitous in our modern world. Many industrial and scientific applications rely on components and instruments made of hard materials to prevent them from breaking or wearing. However, even the strongest and hardest components eventually wear or break and need to be replaced. Usually, the harder a material is, the longer it lasts. For this reason, researchers all over the world are investigating how to improve the hardness of existing materials. In fact, this has been a human tradition ever since Bronze Age civilizations improved upon the hardness of copper by alloying it with tin. In this project, much like our ancestors thousands of years ago, we will be investigating methods for improving the hardness of metals.

It is worth it to take some time to clarify what exactly is meant by a material's hardness in this context. Hardness here refers specifically to the surface of a material and that surface's ability to resist any deformation when it's indented by some sharp object. Hardness is an experimentally observed quantity that is measured in a precisely defined test. Hardness tests are typically performed by pressing an indenter with exactly defined dimensions into the material that is to be tested under a specifically defined load. The hardness is then determined by measuring the depth or size of the indentation left in the material after the test. For example, a commonly used test is the Vickers hardness test, which uses a diamond indenter with a square-based pyramid shape with strictly defined angles. Similar to pressure, one can express hardness in GPa units, but it's important to distinguish it from pressure. Hardness is the load over the surface area of the indentation, while pressure is the load over the area normal to the force.

By using a hardness test like the one described in the previous paragraph, it's possible to determine which materials are the hardest. The material that scores the highest on the Vickers hardness scale is diamond, which, depending on factors like the purity of the diamond, can range anywhere between 70 and 150 GPa. This extremely high hardness is, of course, the reason we typically use diamond indenters to perform Vickers hardness tests. Diamond-like structures that include boron and nitrogen, which have a similar atomic size to carbon, can also be extremely hard. Cubic boron nitride is such a material with a hardness between 40 and 55 GPa [36]. Metal borides are some of the hardest metal compounds that are not insulators or semiconductors. They are made when dense metals like osmium, tungsten, or rhenium are mixed with boron. One common problem with all of these hard crystalline materials is that they pose serious challenges for the synthesis, processing, and shaping of the material. Making components out of them is often not feasible due to high manufacturing costs, limitations in size, or lack of fine control over the shape. Besides this, it's also not always possible to find superhard materials that meet certain requirements when it comes to other properties of the material, like magnetic, electric, or thermal properties. It is for these reasons that components made of conventional metallic alloys are still so ubiquitous in countless industrial applications.

There is still a world of difference in the hardness of various metallic alloys, ranging from just a couple hundred MPa up to tens of GPa on the Vickers hardness scale. Of course, the elemental makeup of the alloy plays an important role here. Pure copper is less hard than pure iron, just to name an example. However, it is not always possible to simply switch to an entirely different alloy to improve the hardness of a component in the hope of making it more wear resistant. Changing the chemical composition of an alloy can require the addition of different elements that can be more expensive, in short supply, or less sustainable to mine. Changing the chemical makeup is not the only way one can modify the material properties of an alloy and potentially increase its hardness. There exist multiple common ways in which alloys can be made significantly harder without affecting the raw materials required to produce them. Many alloys' hardness increases after heat treatment or work hardening the alloy. And steel can be hardened by quenching (rapidly cooling) and tempering the metal. All these different hardening methods have something in common: they all rely on the introduction of crystal defects in the material.

1.2 Metallic Glasses

This idea of frustrating the crystal structure of a material to obtain new properties can be taken to the extreme. We can imagine a material made up entirely of metal atoms arranged in a completely amorphous, disordered way. Figure 1 shows in a schematic way what such an arrangement of atoms can look like. Such a material is often referred to as a metallic glass because its atomic structure resembles that of a glass. And these metallic glasses are not just hypothetical materials; there are well-known methods for producing metallic glass ingots with sizes in the order of centimetres.

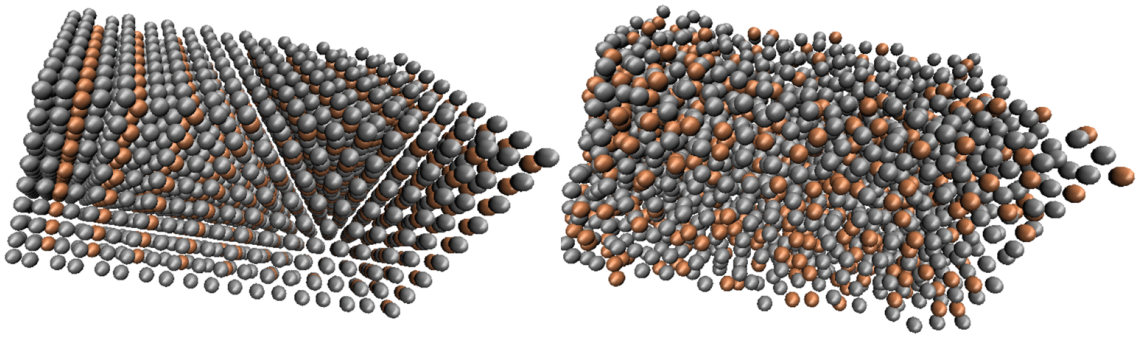

Figure 1: Comparison of a crystalline atomic structure on the left and an amorphous atomic structure on the right.

A common method for producing metallic glass centres around drastically increasing the rate at which an alloy is cooled down after being cast. If the cooling rate is sufficiently high, the atoms will not have enough time to arrange in an ordered crystal structure before the temperature drops so far below the melting point that the atoms lose their mobility. Instead of the regular transition from a fluid to a crystal, the metal goes through what's known as a glass transition and ends up in a completely amorphous, metallic glass phase instead.

Metallic glasses are far from new. W. Klement Junior, R. H. Willens, and P. Duwez reported the first metallic glass over 60 years ago, in 1960. The metallic glass in question was formed by cooling a gold-silicon alloy at a cooling rate in the order of 10^6 Kelvin per second. Only thin sheets or ribbons less than a millimetre thick can achieve such high cooling rates. In the years that followed, more and more alloys were shown to be glass-forming. Some still formed glasses at far lower cooling rates in the order of 100 Kelvin per second [41]. These metallic glasses can form larger ingots, up to several centimetres in diameter, due to their significantly lower cooling rates. Such metallic glasses are commonly referred to as bulk metallic glasses because of their ability to form amorphous structures deep in the bulk of an ingot.

Central to this project is the concept that metallic glasses are regularly harder than their crystalline counterparts [46, 28, 40]. In other words, an alloy could become harder than its crystalline phase if it is prevented from forming a crystal structure, either by rapid cooling or other methods, and left in an amorphous phase instead. Thus theoretically any existing crystalline alloy currently available could be made harder by turning it from a crystalline material into a metallic glass. A basic explanation for why metallic glasses can be harder than their crystalline counterparts is that the lack of long-range order hinders the atoms' mobility, which enhances the material's resistance to plastic deformation. However, the exact mechanisms behind the hardening are complex, and it is generally impossible to know a priori if a metallic glass made from a specific alloy will actually be harder than its crystalline counterpart, let alone by how much. With no reliable prediction from theory for the change in hardness, the only approach is to try each and every possible alloy composition and test the hardness of the metallic glass made from that alloy. This is exactly the main goal of this thesis. To map out, over a broad range of elemental compositions, how hard a metallic glass made of that alloy would be compared to a regular polycrystalline material made of the same alloy.

1.3 Molecular Dynamics

As previously mentioned, the goal of this project is to determine the hardness of metallic glasses compared to their crystalline counterpart over a broad range of elemental compositions. One method to investigate this question would be to go to the lab, melt alloys of various elemental compositions, cool them either slowly to form a regular crystalline structure or rapidly to form a metallic glass, confirm the presence or lack of crystalline structure using x-ray diffraction experiments, and measure the hardness using a hardness test such as the Vickers hardness test. However, such an approach would be severely limited in the compositional space that can be explored because cooling rates are limited by current technology, and many alloys are unable to be turned into metallic glasses at the cooling rates that can currently be achieved in a lab setting. Furthermore, the cost and time required for manufacturing and testing such a large quantity of ingots would be prohibitively high. It is for these reasons that in situations like this it is often worthwhile to first perform computer simulations before committing to performing physical experiments. Computer simulations can have arbitrarily high cooling rates, and thus they allow for the inclusion of metallic

glasses that aren't possible to create in practice. This results in a much broader range of chemical compositions over which the hardening effect of switching from crystalline to amorphous structures can be investigated, potentially revealing more about the nature of this hardening than a physical experiment could. Eventually any conclusions drawn from the theoretical computer simulations will need to be verified by physical experiments in the lab. Effectively, the initial computer simulations work to guide the physical experiments that will need to be performed later, resulting in a far more efficient research process. This thesis project will only be about the initial computer simulations. The simulations will look at the hardness of alloys with crystalline and amorphous structures over a wide range of chemical compositions.

Various simulation techniques exist for predicting materials' elastic properties, such as hardness. In this project the method of choice is a molecular dynamics (MD) approach. In molecular dynamics, atoms are modelled as point particles, and an interatomic force field is defined that describes the current force on each atom based on all the atomic positions in the simulation. Newtonian equations of motion are solved in discrete time intervals. With small enough time intervals, realistic atom trajectories are obtained, and a chunk of material can be simulated over time. Molecular dynamics does not directly simulate the electrons, unlike techniques like density functional theory (DFT). This might seem problematic since one can expect the electrons to play a crucial role in determining the elastic properties of a material. The central idea of molecular dynamics theory is that the influences of the electrons are captured in the interatomic potential. Interatomic potentials can have complicated mathematical forms with many tuneable parameters. Usually, the parameters are fitted such that MD simulations performed using the interatomic potential reproduce experimental observables such as, for example, lattice spacings and angles, densities, or melting points. A molecular dynamics approach is highly favourable over a DFT approach for simulating metallic glasses specifically because a DFT approach is not suitable for simulating both a large number of atoms and a large number of time intervals, which are both needed to accurately simulate metallic glasses. This is because amorphous structures need to be simulated with a large number of atoms in order to eliminate significant periodicity in the simulation and, more importantly, because realistic metallic glass structures need to be obtained by simulating the formation process of a molten alloy cooling down rapidly through time. In this project, basic elastic properties like bulk and shear moduli are extracted from the molecular dynamics simulations, which are then linked to a hardness prediction using empirical hardness models. The exact methodology is described further down in this text in sections 4 and 7.

1.4 Cu-Zr-Al

The alloys investigated in this thesis belong to the Cu-Zr-Al system. This system has been selected due to a combination of well-established glass-forming ability, theoretical predictability, and practical significance in the field of metallic glasses. The Cu-Zr binary system, in particular, is known for its numerous well-characterized glass-forming compositions [31], making it an ideal benchmark for evaluating theoretical predictions against experimentally validated data from existing literature. This strong foundation of prior research ensures that any new insights gained from this study can be meaningfully contextualized within the broader scientific discourse.

The inclusion of aluminium in this system is a logical extension, as it enhances glass-forming ability by disrupting long-range atomic order and inhibiting crystallisation kinetics. Since aluminium atoms are significantly lighter and smaller than copper and zirconium atoms, they can occupy interstitial positions, reducing the critical cooling rate required for amorphous structure formation. This facilitates the formation of bulk metallic glasses (BMGs) with superior mechanical and functional properties. Furthermore, empirical evidence supports the glass-forming potential of Cu-Zr-Al alloys, as multiple compositions within this system have been experimentally verified to form metallic glasses [38, 49]. By systematically studying this system, we aim to deepen our understanding of the underlying mechanisms governing glass formation and stability, ultimately contributing to the broader field of advanced metallic materials.

In this thesis, hundreds of molecular dynamics simulations of many known crystalline structures and their metallic glass counterparts in the Cu-Zr-Al system are performed, and predictions for their hardness are obtained. The exact mechanisms behind the hardening of alloys when they are turned from a crystalline into an amorphous material are not well known. By determining the magnitude of this hardening over a large range of chemical compositions, a deeper understanding of the hardening effect might be obtained, aiding in the search for ever harder materials. In doing so, this project also provides a general framework for using MD simulations to study the hardness of metallic glasses of almost any chemical composition.

1.5 Previous Work

The earliest examples of metallic glasses were thin films of atoms deposited at very low temperatures [5]. But metallic glasses really came to prominence after 1960, when Klement, Willens, and Duwez rapidly cooled gold-silicon alloys using a technique known as splat quenching [22]. These authors used an x-ray diffraction pattern to show that an amorphous structure was formed in 25 atomic percent of the gold-silicon alloy. In the years that followed, researchers used the splat quenching technique to study the formation of metallic glasses in alloys with varying chemical compositions. In 1976, a new cooling technique using a supercooled fast-spinning wheel led to the discovery of Fe-Ni-B metallic glass [26], which came to be known commercially as "metglas." The list of glass-forming alloys continued to expand with the development of more and more cooling techniques. Commonly found glass-forming alloys these days are mostly Zr-based, Fe-based, Co-based, Ni-based, Cu-based, or Pd-based [41].

Metallic glasses are interesting from a theoretical standpoint. Metallic glasses can be used as example systems to learn more about the glass transition, one of the unresolved critical issues in solid-state physics and materials science [20]. But metallic glasses also pose interesting questions of their own, mainly concerning the reason for the difference in the critical cooling rate of different chemical compositions. Alloys with lower critical cooling rates can be cast in ingots of larger diameter while remaining fully amorphous throughout, which makes them more applicable for science and engineering purposes. It is known that adding many different elements of different sizes lowers the critical cooling rate; this phenomenon is also referred to as the confusion principle [15]. An excellent example of the concept is the Zr-Ti-Cu-Ni-Be metallic glass discovered by Peker and Johnson in 1993[39]. But this is certainly not the whole story because certain elements simply form metallic glasses more easily than others without a clear explanation as to why. For instance, scientists had a hard time finding metallic glasses with a lot of aluminium until 1988, when Al-based metallic glasses with a transition metal and a lanthanide were suddenly shown to be great at making glasses [18].

Besides being intriguing from a theoretical viewpoint,, metallic glasses are also intriguing from an engineering/societal standpoint. Known for their amorphous structure and exceptional properties, metallic glasses have diverse applications across various fields. Because they are strong, don't rust, and are biocompatible, they are used in cardiovascular stents, orthopaedic implants, and surgical tools in the biomedical field [41]. Their excellent magnetic properties make them ideal for transformers, inductors, and magnetic shielding in electronics [52]. Additionally, metallic glasses are employed in precision components for consumer electronics, wear-resistant coatings for cutting tools, and high-strength lightweight materials for aerospace and sports equipment [27, 40]. Their unique thermal and electrical characteristics also support applications in energy storage, catalysis, and hydrogen storage. [17] In short, metallic glasses have many key advantages over their crystalline counterparts. They are often stronger, have a higher yield strength, are more resistant to corrosion, and most importantly for this current project, metallic glasses are often harder than crystalline alloys [40, 15, 41, 46, 28].

This brings us back to the central question of the project: how much harder exactly are metallic glasses compared to their crystalline counterparts? This is different for different chemical compositions of alloys, so one would ideally want to study a wide range of glasses of varying composition to answer this question. Physical experiments that study a large range of metallic glasses have been done before. Only a few years ago, Li et al. performed an experiment that included as many as 5700 different alloys from 12 alloy systems [25]. In this experiment, the authors measured X-ray diffraction patterns to study the glass-forming abilities of these metallic glasses. One could imagine performing a similar experiment for this project with the addition of hardness tests performed on all the samples. However, as we discussed in section 1.3, this project instead takes a molecular dynamics modelling approach. This way, metallic glasses that are not possible to create with current technologies can still be included, and a large compositional space can be screened for hard materials in a very efficient way.

As mentioned, a central ingredient in this study is a dataset of the hardness of metallic glasses over a broad range of chemical compositions obtained by way of computer simulations. More specifically, we make use of molecular dynamics simulations and have restricted ourselves to alloys in the Al-Cu-Zr system. Molecular dynamics has been widely used to study metallic glasses in this system. For example, there have been many studies that looked at the glass-forming ability of glasses in Cu-Zr alloys [48, 43] as well as Al-Cu-Zr alloys [7, 50]. Obtaining hardness values from a molecular dynamics simulation can be challenging. One could fully replicate a nanoindentation experiment by simulating the impact of a solid ball on the surface of a metallic glass structure just like the polycrystalline copper simulation performed by Alexey Bolesta in 2019 [4]. Such simulations

are often computationally expensive however and so they run the risk of severely limiting the total number of chemical compositions we can perform a simulation of. It has been shown that there is a strong correlation between a material's hardness and that material's bulk and shear moduli [6]. This offers a way to use bulk and shear moduli to screen for hard materials. Relatively computationally cheap methods exist to obtain the bulk and shear moduli from molecular dynamics simulations by directly measuring stress-strain relations during the simulation [8, 29]. And many studies exist that report experimentally obtained values for these stress-strain relations, sometimes represented as a set of elastic stiffness constants, in the Cu-Zr-Al system that the molecular dynamics results can be compared to [11, 31, 37, 38, 42, 49, 51]. The bulk and shear moduli can then be fed into one of the widely used empirical hardness formulas [44, 6, 45] to predict the hardness of the simulated material [2].

In Klement, Willens, and Duwez's 1960 paper, the authors use X-ray diffraction experiments to show that a non-crystalline structure was formed [22]. X-ray diffraction experiments are a commonly used tool for studying metallic glasses. Its applications extend beyond merely demonstrating the formation of a non-crystalline structure. In 2022 Hui Wang used X-ray diffraction data of some bulk metallic glasses to gain insight into the materials' ductility/plasticity [47]. And in the 2021 Li et al. nature paper, X-ray diffraction again plays a crucial role: the authors link the glass-forming ability of many alloys in glass-forming systems to the full width at half maximum of the first diffraction peak in the diffraction pattern [25]. In molecular dynamics simulations this same information is accessible in the form of pair correlation functions, which can be computed at various points during the simulation and can be used in much the same way as X-ray diffraction data.

1.6 Final Remarks

Metallic glasses are an interesting class of materials with applications ranging from wear-resistant coatings to hip implants. They are widely studied both by means of physical experiments and with computer simulation techniques. A striking property of metallic glasses is their tendency to be harder than their crystalline counterparts. Exactly by how much the hardness of a specific alloy will increase after vitrification remains difficult to predict. Here we present a series of hundreds of molecular dynamics simulations of many known crystalline structures and their metallic glass counterparts in the Cu-Zr-Al system together with theoretical predictions for the metallic glasses' hardness. This way we gain a deeper understanding of the hardening effect of alloy vitrification and, in the process, develop a general framework for using molecular dynamics simulations to study the hardness of metallic glasses.

The next chapter, chapter 2, will include a general discussion of the theory and methods underpinning molecular dynamics simulations, after which we discuss the interatomic potential used for these simulations extensively and provide some methodology on generating metallic glass structures in chapter 3. Further methodology on determining the elastic moduli of the simulated metallic glasses is provided in chapter 4. In chapter 5 it is confirmed through radial distribution functions that the structures generated in the simulations represent amorphous compounds after which the results of the bulk and shear moduli measurements and the corresponding Vickers hardness predictions are presented in chapters 6 and 7 respectively. Two additional chapters are provided at the end: one on a Voronoi tessellation analysis (chapter 8) and another on the effect of the simulated cooling rate (chapter 9), followed by this study's conclusions presented in chapter 10. Extra material is provided in appendix A.

2 Molecular Dynamics Theory

Introduction

At the heart of this project is a method for simulating the motions of atoms called molecular dynamics. In molecular dynamics, atoms are treated as simple point particles with positions and velocities. The simulation time is discretized into small chunks or time steps. Every time step, the forces acting on the atoms are computed. Then the Newtonian equations of motion are solved numerically using some integration algorithm to obtain new particle positions and velocities. By iterating over many time steps the trajectories of atoms in a material are simulated. We will dedicate the rest of this section to an overview of the most important methods and theory for this project concerning molecular dynamics.

Integration Algorithm

The molecular dynamics codes used in this project use an algorithm called velocity Verlet integration to integrate Newtons equations of motion. In the first step of this algorithm the atom velocities are computed half way in the next time step:

$$\vec{v}\left(t+\frac{1}{2}\Delta t\right)=\vec{v}\left(t\right)+\frac{1}{2}\vec{a}\left(t\right)\Delta t \tag{1}$$

Which are then used to compute the atom positions in the next time step.

$$\vec{x}\left(t+\Delta t\right)=\vec{x}\left(t\right)+\vec{v}\left(t+\frac{1}{2}\Delta t\right)\Delta t \tag{2}$$

After this the acceleration on each atom in the next time step is derived from the interatomic potential (more on that in section 3) and finally the atom velocities at the next step are computed as

$$\vec{v}\left(t+\Delta t\right)=\vec{v}\left(t+\frac{1}{2}\Delta t\right)+\frac{1}{2}\vec{a}\left(t+\Delta t\right)\Delta t \tag{3}$$

This method is frequently used to calculate trajectories in molecular dynamics simulations because of it's time reversibility and good numerical stability and it's the one that was implemented in this project.

Temperature and Pressure Control

In the most basic molecular dynamics simulations, the volume, energy, and number of atoms of a system are constant. In the study of thermodynamics, this configuration is known as the microcanonical ensemble. If one wishes to study a system where not energy but temperature is kept constant (the canonical ensemble), a method for controlling the temperature must be implemented. In molecular dynamics this is known as thermostatting. A popular method of thermostating—and the one used in this work—is the Nosé-Hoover thermostat.

In the approach of Nosé and Hoover, a modification is made to the equations of motion in the form of an extra degree of freedom in the Hamiltonian, which represents a virtual heat bath. The effect of the heat bath on the Hamiltonian is such that the atom velocities are reduced when the simulation is hotter than the target temperature, and the velocities are increased when the temperature is below the target temperature. This way the temperature is brought back to the target temperature over time. There is a parameter in the modified Nosé-Hoover Hamiltonian that can be thought of as a damping parameter controlling how aggressive the thermostat brings the temperature back to the target temperature. The ideal value of this parameter is system-specific; too low values will lead to poor temperature control, but setting it too high will cause high-frequency fluctuations of the temperature.

A similar technique can be applied to run isobaric simulations at a set constant pressure. This is done by adding yet another degree of freedom in the Hamiltonian and coupling it not to the atom velocities but to the volume of the simulation box. This way, a pressure above the target temperature will cause the simulation box to expand, bringing it back down to the target pressure. And likewise, a pressure below the target pressure will cause the simulation box to contract. The pressure control also has a damping parameter analogous to the temperature damping parameter.

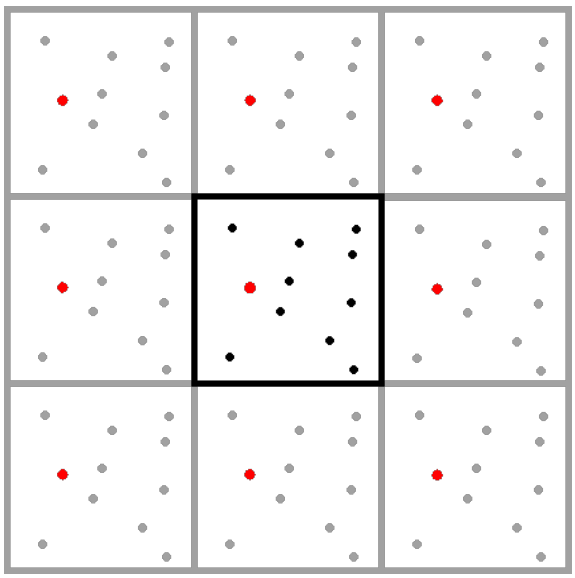

Figure 2: A 2D example of a central primary simulation cell being surrounded by virtual simulation boxes where the atoms have the exact same positions and velocities as in the primary box. This is used to accurately compute the interatomic forces in a molecular dynamics simulation with periodic boundary conditions.

Boundary Conditions

Molecular dynamics simulations are usually restricted to some finite volume, and a decision needs to be made on what happens at the boundaries of the simulation volume. One option is to impose an additional extremely strong potential at the boundaries, restricting the atoms to the simulation box. This has the effect that atoms can bounce off the hard boundary, and the inclusion of these boundary effects can have big consequences for the simulation. Another option, and the one used in this work, is to impose periodic boundary conditions: when an atom goes out of the simulation box on one side, it comes back in at the other side. Periodic boundary conditions simulate the conditions inside the bulk of a material and are ideal for calculating macroscopic properties from relatively few simulated particles. To accurately simulate the forces, one must be mindful of the fact that atoms close to the boundary are actually very close to those close to the boundary on the other side of the simulation box and should therefore experience a force due to their potential. The way this is taken into account in MD simulations can be thought of as having the primary simulation cell be surrounded by virtual image cells, as illustrated in figure 2. These virtual simulation cells have the exact same content in terms of atom positions and velocities as the primary cell. The force on an atom is then computed by looping over all of the atoms, including the ones in the virtual cells, and adding their contributions. Truncating the potential to at least half of the simulation box size ensures that atoms only feel one another once; the force either comes from an atom in the primary cell or from one of its images. Only the forces on the atoms in the primary simulation cell are computed, and after the integration algorithm updates all the atom positions and velocities in the primary cell (potentially moving them to the other side of the primary cell if they leave the boundary), they are copied to the surrounding image cells. The shape of the cells is often cubes or simple rectangular boxes, but in theory any shape that tiles the entire space by pure translation alone can be used, and in fact many of the simulation cells in this project are parallelepipeds and not simply rectangular boxes.

Neighbour List

The force calculations are the most computationally expensive part of a simulation step in a molecular dynamics simulation. For every atom, one needs to loop over all other atoms in the simulation, compute their distances, consult the inter-atomic potential for the force contributions, and then add up all the force contributions to find the total force on that atom. A naive approach would result in N^2 force calculations every timestep. In typical simulations, at any one time only a limited number of atoms are actually within the force cutoff radius and contributing to the force, so the vast majority of the N^2 force calculations will come out as zero. Furthermore, atoms that are close to one another in one timestep are likely to still be close to each other in the next timestep

and vice versa for atoms that are far away. Constructing neighbour lists under these conditions can save a significant amount of computing power.

A neighbour list is simply a list of all the atoms that are within a certain distance. One can consult the neighbour list during force computation to only check atoms that are close to one another, dramatically accelerating the process. Of course, constructing neighbour lists is computationally expensive as it requires checking all N^2 distances to determine which atoms are close and which are far away. The trick is to not update the neighbour list every time step. This does introduce a risk: if an atom that was initially far away enough to not be included in the neighbour list moves within the force cutoff radius, its contribution to the total force will not be counted until after the neighbour list is updated again. To minimise this risk, the neighbour lists should also include atoms that are not within the cutoff distance yet but are close enough that they might end up there before the next neighbour list update. How close is too close? It depends on the specifics of the simulation and on the frequency at which the neighbour lists are updated, and at the end of the day, there is always a balance between computing cost and a risk of inaccurate force computation.

Initialization

So far, all our discussion on molecular dynamics simulations has been about computing the atom positions and velocities in the next time step given the positions and velocities at the current time step. Something that we haven't discussed yet is how we should set atom positions and velocities at the very first time step, when there is no previous time step to compute from. In this project we are mainly concerned with the initialization of crystal structures (of Cu-Zr-Al alloys specifically). If the crystal lattice and the atoms' positions within the lattice are known a priori, either through experimental observation or previous simulations, then this can be used to initialise the atom positions for a new simulation. These positions will typically deviate very slightly from the most stable positions in a simulation, and an equilibration phase is always required at the start of the simulation to ensure a stable structure has been obtained. With the atom positions set according to some crystal structure, that just leaves the atom velocities. Initialisation of the atom velocities typically follows two important rules. Firstly, the velocities must be in accordance with the target temperature in the simulation. For example, this can be achieved by ensuring the velocities follow a Maxwell-Boltzmann distribution corresponding to the given temperature. The second rule is to make sure the total linear and angular momentum are zero, which can be achieved by carefully scaling some of the atom velocities. For systems with a large number of atoms, the total linear and angular momentum are typically already minimal as long as the atom velocities are set to random directions, so this second correction has little effect.

In this project we also implemented a second method of initialising structures, which we refer to as the "randomised initialisation method.". It was designed to allow for the generation of metallic glasses with arbitrary chemical composition. We do this by first generating a cubic lattice of 10,000 atom positions. Then we randomly assign elements to these atom positions with some specified ratio. For example, say the desired metallic glass composition is 2:1:1 for Al:Cu:Zr; then 5000 randomly selected atom positions will be assigned Al, another 2500 will be assigned to Cu, and the remaining 2500 will be assigned Zr. While the structures initialized this way are entirely unrealistic they are useful because by increasing the temperature to far above the melting point we can obtain a simulation of a molten alloy of any desired chemical composition. This capability in turn lets us generate metallic glass structures with element ratios different from the element ratios present in the various crystal structures discussed in the previous paragraph.

Static Properties

We will close out this section by discussing how some thermodynamic quantities can be computed from a molecular dynamics simulation. Typically, these quantities are computed as time averages of some function of the particle positions and velocities. For example the average potential and kinetic energy in the system is computed by taking the time average of their instantaneous values

$$V(t) = \sum_i \sum_{i>j} U(\vec{r_{ij}}) \tag{4}$$

$$K(t) = \frac{1}{2} \sum_i m_i v_i^2 \tag{5}$$

where $U(\vec{r_{ij}})$ represents the potential between atoms i and j and m_i and $\vec{v_i}$ are the mass and velocity of atom i. The instantaneous temperature of the system can be related to the total kinetic energy in the system through the equipartition theorem

$$K = \frac{3}{2} N k_B T \iff T = \frac{2K}{3Nk_B} \tag{6}$$

where N is the total number of atoms in the system and k_B is the Boltzmann constant. Finally, the virial theorem offers an expression for the instantaneous pressure in terms of known quantities in the system as

$$P = \frac{NK_BT}{V} + \frac{1}{3V} \sum_i \vec{r_i} \cdot \vec{f_i} \tag{7}$$

where $\vec{r_i}$ is the position of atom i and $\vec{f_i}$ is the force acting on atom i. Since the atoms' positions, velocities, potential interactions, and total forces have to be computed every time step anyway, it is not much more computationally expensive to compute quantities like pressure, temperature, and energy during a simulation run.

3 Simulating Cu-Zr-Al Metallic Glass in MD

To compute the forces on the atoms, we make use of an interatomic potential. Interatomic potentials provide the potential energy of a system of atoms as a function of their position. We can compute a force by differentiating the interatomic potential with respect to the atom position. Many different forms of interatomic potentials exist. These range from simple two-body pair potentials like the Lennard-Jones potential to more complex many-body potentials like the embedded atom model. In molecular dynamics, a simulation is only as good as the interatomic potential used to model the interactions between the atoms. If one does not use an appropriately well-fitted potential that is applicable to the problem, the outcome of the simulation will be of very little value. Therefore, a lot of care must be taken when picking the potential. We divide this section into three parts. In the first part, various Cu-Zr potentials available in literature are discussed and compared. The second part discusses the creation of a tertiary Cu-Zr-Al potential from three constituent binary potentials to allow for the inclusion of aluminium in the simulations. In the final subsection, we will discuss how a number of important simulation parameters were set.

3.1 Review of Cu-Zr Potentials

In this section, we will examine and contrast several Cu-Zr interatomic potentials intended for use in molecular dynamics simulations. After searching the literature, four Cu-Zr potentials came under consideration. The text will refer to these as "Kobayashi1980," "Kim2008," "Mendelev2009," and "Mendelev2019."

The first potential, referred to in this work as 'Kobayashi1980', was developed by S. Kobayashi in 1980 [23] and it's functional form is what's known as a Lennard-Jones potential. Lennard-Jones potentials are no doubt the most extensively studied type of interatomic potential. They are simple two-body potentials with one attractive and one repulsive term, both of which approach zero as the distance between atoms approaches infinity. Typically the repulsive term goes as r^{-12} while the attractive term goes as r^{-6}. This form elegantly captures the expected behaviour of atoms repelling each other at short distances, attracting each other at further distances, and not interacting at infinite distances. The model, however, does not capture directional forces and many-body effects that may be involved in real atomic interactions. The kobayashi1980 potential is a slightly modified version of the standard Lennard-Jones potential with a r^{-8} repulsive term and a r^{-4} attractive term. The parameters of the Cu-Cu and Zr-Zr interactions were set such that the model accurately predicted the fcc lattice spacings and cohesive energies for pure copper and pure zirconium. For the mixed Cu-Zr interactions, parameters were typically averaged between the pure Cu and pure Zr values. For more details as well as exact parameter values, we refer to the original 1980 paper. Kobayashi used this potential to simulate a $Cu_{57}Zr_{43}$ metallic glass made of 1533 atoms. He computed the elastic constants and showed that they agreed well with the experimentally observed Young's and shear modulus of $Cu_{57}Zr_{43}$ metallic glass.

The second potential, 'Kim2008,' is a modified embedded atom method (MEAM) potential developed by Young-Min Kim and Byeong-Joo Lee in 2008 [3, 21]. The MEAM potential, especially the second nearest neighbour MEAM, has been very successful in accurately modelling metallic compounds with various elemental compositions and crystal structures while maintaining a common mathematical formalism. The original embedded atom method approximates the local electron density at each atom's location. The modified embedded atom method adds directional forces to this. MEAM balances computational efficiency with the ability to model a wide range of materials like metals, semiconductors, and even some gaseous elements. With this added complexity, however, also comes more free parameters and a higher reliance on empirical data needed for fitting all these parameters. Similarly to the Kobayashi1980 potential, the pure copper and pure zirconium parts of the potential were fitted to accurately predict the physical properties of these pure systems. The parameters for the Cu-Zr interactions were not just simple averages of the pure Cu and Zr cases, but rather they were fitted to accurately predict some properties of the B2 $CuZr$ and $C11_b$ $CuZr_2$ crystal phases of the Cu-Zr alloy system. For more details on the fitting procedure, we again refer to the original paper. In the paper, the authors also demonstrate the applicability of the potential to studying the mechanical and deformation behaviour of Cu-Zr metallic glasses.

We looked at two more potentials in this study. They are called Mendelev2009 and Mendelev2019. They are Finnis-Sinclair (FS) type potentials [1, 16]. FS potentials mimic the second-moment approximation of tight-binding theory, where the cohesive energy is linked to the square root of the coordination number. This represents the density of electronic states around an atom. The form is particularly well-suited for transition metals due to the significant role of dd-electrons in bond-

ing. Therefore, people have extensively used these potentials to simulate defect dynamics, surface phenomena, and mechanical properties of metals, including modelling vacancies, dislocations, and grain boundaries. There is no directionality in bonding in FS potentials, and just like in MEAM potentials, there is a strong reliance on fitting data, meaning the potential's performance can degrade outside the parameterised range. The original version of the Cu-Zr FS potential was created in 2009 [33]. It was the first of the four potentials considered in this study that was directly fitted to properties of amorphous structures that were observed in experiments, instead of only fitting to crystal structures. Specifically, the parameters of this model were chosen such that simulations of $Cu_{64.5}Zr_{35.5}$ metallic glass produced diffraction data that was in good agreement with the experiment as well as accurate densities for the liquid phase over a range of temperatures. The model resulted in a significantly more accurate prediction of the glass transition temperature, suggesting that this potential is better suited to study the vitrification of copper zirconium metallic glasses. In 2019 a slight modification to the potential was made [32] after simulations performed at a relatively low cooling rate showed that the original 2009 potential overestimated crystallisation speed.

To compare the various Cu-Zr potentials available in literature, a selection of Cu-Zr crystal structures was simulated using the General Utility Lattice Program (GULP). GULP was originally developed in 1997 and can be used to compute basic material properties of a crystal system when given a lattice and an interatomic potential. We used GULP to compute the lattice constants and angles, bulk and shear moduli, and the density of pure copper and pure zirconium, as well as four experimentally observed crystal structures in the $Zr_{14}Cu_{51}$, Zr_3Cu_8, Zr_7Cu_{10}, and Zr_2Cu alloys. The comparison of the various potentials was done as follows: First, the simulation was set up using precise lattice information from the materials project database [19]. Then the GULP code was used to relax this initial structure. During relaxation, the atom positions are varied slightly until the internal energy of the system is minimised. The internal energy is computed using one of the four interatomic potentials discussed in this section, and the slight differences between these potentials result in slightly different atom positions after relaxation. The GULP code also outputs values for the density as well as the bulk and shear modulus. The results from these computations are shown in table 1.

Table 1 also lists reference values for the various computed properties under the column "ab initio.". The lattice information and elastic properties listed in the materials database all come from either direct observation (Cu, Zr, Zr_3Cu_8, and Zr_2Cu lattices) or higher-level density functional theory calculations ($Zr_{14}Cu_{51}$ and Zr_7Cu_{10} lattices and bulk and shear moduli) and thus serve as a good reference point to judge the relaxed GULP structures against. The DFT computations performed for the material project database employ a mix of Generalised Gradient Approximation (GGA), GGA+U, and r2SCAN, implemented in the Vienna Ab Initio Simulation Package (VASP) software. Input structures for the DFT relaxation are sourced from many different places. For more information on the source of the experimental data, see the material project paper [19].

From the values in table 1, it is immediately obvious that the Kobayashi1980 potential is ill-suited to compute material properties like bulk and shear moduli, as it overestimates these values by more than a factor of two in all cases where these properties were computed. Such behaviour is expected since the extremely basic pair potential form of the Lennard-Jones potential neglects many-body effects and is only really a good approximation for spherical and simply dispersively interacting molecules. The remaining three potentials all perform well in the lattice spacings and angles, never being more than a few percent off the ab initio calculations. Kim2008 outperforms Mendelev2009 and Mendelev2019 in the bulk and shear moduli of all three of the structures for which these quantities were computed. The difference is most clear in the Zr2Cu structure: Mendelev2009 greatly underestimates both the bulk and shear moduli, while Mendelev2019 gives nonphysical results for the Reuss shear modulus. On the other hand, Kim2008's potential is less than 1% off for the bulk moduli and has a reasonably good agreement for the shear moduli as well. Given how central computing elastic moduli of intermetallic structures is to this project, the decision was made to include the Kim2008 potential.

Table 1: Lattice spacings and angles, bulk and shear moduli, and densities of various copper-zirconium crystal structures. The first column lists previously reported DFT values (see [19] [9]), and the other four columns contain our results from molecular dynamics simulations with four different interatomic potentials. [23] [21] [33] [32]

Cu		ab initio	Kobayashi1980	Kim2008	Mendelev2009	Mendelev2019
lattice spacings (Å)	a	2.53	2.46	2.56	2.57	2.57
	b	2.53	2.46	2.56	2.57	2.57
	c	2.53	2.46	2.56	2.57	2.57
lattice angles (deg)	α	60	60	60.00	60.00	60.00
	β	60	60	60.00	60.00	60.00
	γ	60	60	60.00	60	60
bulk modulus (GPa)	V	139	486.49	141.99	145.13	143.39
	R	139	486.49	141.99	145.13	143.39
	VHR	139	486.49	141.99	145.13	143.39
shear modulus (Gpa)	V	53	291.89	59.31	61.05	59.99
	R	29	237.00	43.57	43.14	41.22
	VRH	41	264.45	51.44	52.09	50.61
density (g/cm$\hat{3}$)		9.22	10.08	8.95	8.76	8.76
Zr14Cu51		ab initio	Kobayashi1980	Kim2008	Mendelev2009	Mendelev2019
lattice spacings (Å)	a	11.27	10.63	11.11	11.55	11.28
	b	11.27	10.63	11.11	11.55	11.28
	c	8.34	8.00	8.55	7.97	8.40
lattice angles (deg)	α	90	90	90.00	90.00	90.00
	β	90	90	90.00	90.00	90.00
	γ	120	120	120.00	120.00	120.00
bulk modulus (GPa)	V	-	623.05	136.03	155.67	136.76
	R	-	622.17	136.03	146.53	136.56
	VHR	-	622.61	136.03	151.10	136.66
shear modulus (Gpa)	V	-	284.63	56.64	44.70	30.32
	R	-	282.48	56.46	42.50	29.02
	VRH	-	283.56	56.55	43.60	29.67
density (g/cm$\hat{3}$)		8.18	9.58	8.21	8.14	8.11
Zr3Cu8		ab initio	Kobayashi1980	Kim2008	Mendelev2009	Mendelev2019
lattice spacings (Å)	a	7.95	7.61	7.83	8.05	7.87
	b	8.23	7.85	8.21	8.23	8.42
	c	10.08	9.66	10.04	9.92	10.04
lattice angles (deg)	α	90	90	90.00	90.00	90.00
	β	90	90	90.00	90.00	90.00
	γ	90	90	90.00	90.00	90.00
bulk modulus (GPa)	V	-	503.26	133.73	147.73	137.73
	R	-	503.14	133.68	146.13	137.36
	VHR	-	503.20	133.71	146.93	137.55
shear modulus (Gpa)	V	-	243.08	44.00	38.31	33.42
	R	-	234.31	43.54	37.83	29.96
	VRH	-	238.69	43.77	38.07	31.69
density (g/cm$\hat{3}$)		7.87	9.00	8.05	7.90	7.81
Zr7Cu10		ab initio	Kobayashi1980	Kim2008	Mendelev2009	Mendelev2019
lattice spacings (Å)	a	9.31	9.09	9.42	9.30	9.20
	b	7.86	7.50	7.79	7.95	7.98
	c	7.86	7.50	7.79	7.95	7.98
lattice angles (deg)	α	72.37	76.12	75.14	71.60	70.36
	β	90	90	90.00	90	90.00
	γ	90	90	90.00	90.00	90.00
bulk modulus (GPa)	V	-	503.03	124.35	161.25	163.47
	R	-	503.02	124.35	154.22	163.28
	VHR	-	503.02	124.35	157.74	163.38
shear modulus (Gpa)	V	-	260.54	72.26	54.49	56.67
	R	-	230.34	71.75	51.05	54.85
	VRH	-	245.44	72.00	52.77	55.76
density (g/cm$\hat{3}$)		7.73	8.53	7.65	7.58	7.68
Zr2Cu		ab initio	Kobayashi1980	Kim2008	Mendelev2009	Mendelev2019
lattice spacings (Å)	a	3.22	2.97	3.26	3.22	3.14
	b	3.22	2.97	3.26	3.22	3.14
	c	6.04	5.69	5.91	5.93	6.21
lattice angles (deg)	α	105.48	105.10	105.98	105.74	104.60
	β	105.48	105.10	105.98	105.74	104.60
	γ	90	90	90.00	90.00	90.01
bulk modulus (GPa)	V	109	749.40	109.57	81.25	83.30
	R	109	745.57	109.55	77.63	64.45
	VHR	109	747.48	109.56	79.44	73.88
shear modulus (Gpa)	V	50	422.91	48.35	35.11	38.43
	R	45	349.50	41.24	23.06	-47.48
	VRH	47	386.21	44.80	29.08	-4.53
density (g/cm$\hat{3}$)		7.04	8.78	7.07	7.21	7.15
Zr		ab initio	Kobayashi1980	Kim2008	Mendelev2009	Mendelev2019
lattice spacings (Å)	a	3.24	3.05	3.23	3.22	3.22
	b	3.24	3.05	3.23	3.22	3.22
	c	5.17	4.89	5.14	5.22	5.22
lattice angles (deg)	α	90	90	90	90	90
	β	90	90	90	90	90
	γ	120	120	120	120.00	120.00
bulk modulus (GPa)	V	94	529.28	96.78	99.41	99.23
	R	94	528.49	96.73	99.30	99.11
	VHR	94	528.88	96.75	99.35	99.17
shear modulus (Gpa)	V	35	286.27	40.92	44.01	43.86
	R	33	275.95	40.53	42.12	41.93
	VRH	34	281.11	40.72	43.06	42.90
density (g/cm$\hat{3}$)		6.45	7.66	6.54	6.47	6.47

3.2 Development of Cu-Zr-Al MEAM Potential

This section details the steps taken to acquire a potential capable of describing the inter-atomic forces in the tertiary Cu-Zr-Al system. Such a potential poses a challenge as no potential is readily available in literature that includes all three elements and all their interactions. However, a literature search did produce several aluminium-copper and aluminium-zirconium potentials. To be able to simulate alloys where all three elements are present at the same time, the binary Cu-Zr, Al-Cu, and Al-Zr potentials were combined to form one Al-Cu-Zr interatomic potential. This is possible in theory because one can model the Cu-Zr interactions using one potential while modelling the Al-Zr interactions with another, etc. There are, however, drawbacks to constructing a tertiary potential in this way. Firstly, the potential parameter fitting procedure inevitably does not include any experimental data taken from compounds that contain all three element species. This is because all parameters in the combined potential originate from the constituent binary potentials whose fitting procedures only included compounds in the corresponding binary element systems. Secondly, the binary potentials might be of a different mathematical form. The mixing of potentials with different physical ideas and assumptions underpinning them is to be avoided, as it makes it impossible to judge whether the potential has suitable assumptions for a given problem, and it makes interpreting the physical meaning of the parameters in the potential impossible. Another thing to consider is that even when potentials use the same mathematical framework, their fitting procedures will generally still be different, which could negatively impact the accuracy of the combined potential. For example, combining a potential that was only fitted to accurately predict melting points and a potential that was only fitted to predict the bulk modulus accurately might produce a combined potential that does not perform well in either task.

After searching the literature, only a single potential was found for the aluminium-zirconium alloy system. It is a MEAM-type potential developed by R. Fereidonnejad et al. in 2022 [12]. Since it is a MEAM potential, it is in theory suitable to be combined with the Kim2008 copper-zirconium potential discussed earlier. This potential is fitted to reproduce lattice parameters, formation enthalpies, elastic moduli, coefficients of volume thermal expansion, and melting points of various intermetallic crystal phases in the Al-Zr alloy system. To complete the full tertiary Al-Cu-Zr potential, a MEAM-type aluminium-copper potential is needed. Such a potential was developed by Avik Mahata et al. in 2022 [30]. It was fitted to reproduce accurate fcc/bcc/hcp energies, lattice parameters, bulk moduli, elastic constants, vacancy formation energies, and stacking fault energies.

With that, all the Cu-Zr, Al-Cu, and Al-Zr interactions can be described by their respective MEAM binary potential, allowing them to be combined into a tertiary Al-Cu-Zr potential. One more problem is that the three binary potentials have slightly different parameter values for the parts of the potentials that describe the interactions between Al and Al, Cu and Cu, and Zr and Zr. For each of these interactions, the parameter values were averaged between those of the two relevant binary potentials. For instance, the parameters related to the Al-Al interactions were derived from the average of the Al-Zr and Al-Cu potentials.

The full list of MEAM parameter values used for the Cu-Zr-Al potential developed this way can be found in appendix A.3. Again, we refer to the relevant papers [3, 12, 30, 21] for more details on the mathematical description of the MEAM potential and the exact parameter values of all the potentials used in the project.

3.3 Simulation Parameters

This project is concerned with comparing alloys' crystalline and amorphous phases. For each alloy included in the scope of the project, the atomic structure of the crystalline phase was readily obtained from experimental measurements and ab initio relaxation calculations thanks to the materials project database [19]. The atomic structure of the amorphous phase was then obtained from the crystalline one by simulating a melt-quench experiment in a molecular dynamics simulation. In a melt-quench experiment a piece of material is first heated to above it's melting point to make it liquid and then cooled back down rapidly (quenched). With sufficiently high cooling rates, no crystallisation occurs, and the material ends up in an amorphous state. This project's molecular dynamics simulations replicated a melt-quench procedure in five steps. First, a crystal structure is initialised and given time to relax to a stable state. The next step involves raising the temperature from room temperature to a temperature significantly above the melting point. This is followed by another relaxation period. In the fourth phase, the simulation temperature is brought back down to room temperature rapidly. The simulation ends with a final relaxation step. Figure 3 shows how the temperature in a typical simulation changes over time.

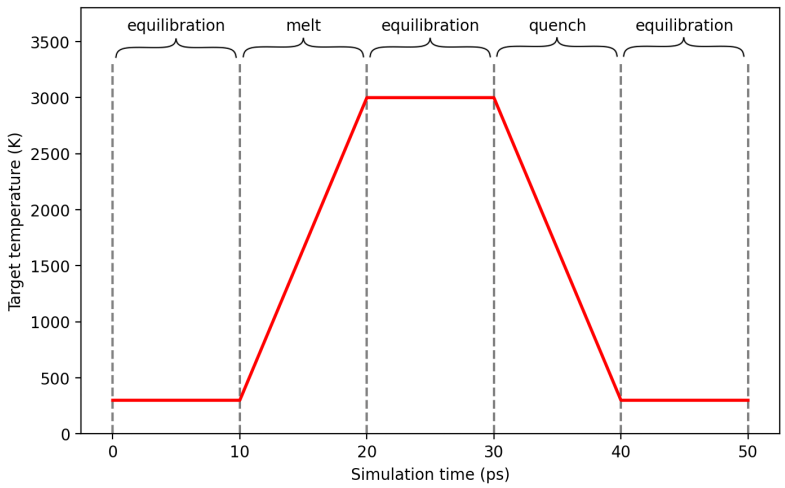

Figure 3: An example of how the target temperature in K changes over the course of a melt-quench simulation. The target temperature in K is plotted against the simulation runtime in ps. During this 50 ps simulation, the temperature is increased from 300 to 3000 K and then cooled back down to 300 K. The various phases are indicated at the top. There are three equilibration phases where the temperature is kept constant with melting and cooling (quenching) phases in between.

Molecular dynamics simulations such as these typically involve a great number of parameters that need to be set to appropriate values. Matters such as the duration of a time step, the total number of atoms in the simulation, and the way the temperature and pressure are controlled all need to be specified in the code. Often there is a balance between simulation accuracy and computing cost when deciding these parameters. For example, a simulation with only a hundred atoms might run very fast but produce inaccurate results. But on the other hand, it would be a waste to simulate tens of millions of atoms if the results are the same as a much faster simulation with only a hundred thousand atoms. Generally, the preferred method in these cases is to test a range of different values, determine at which point the value of the parameter no longer affects the outcome, and choose that value to be used for any future simulations. Figure 4 shows how the atom count was selected in this way for the simulations in this project.

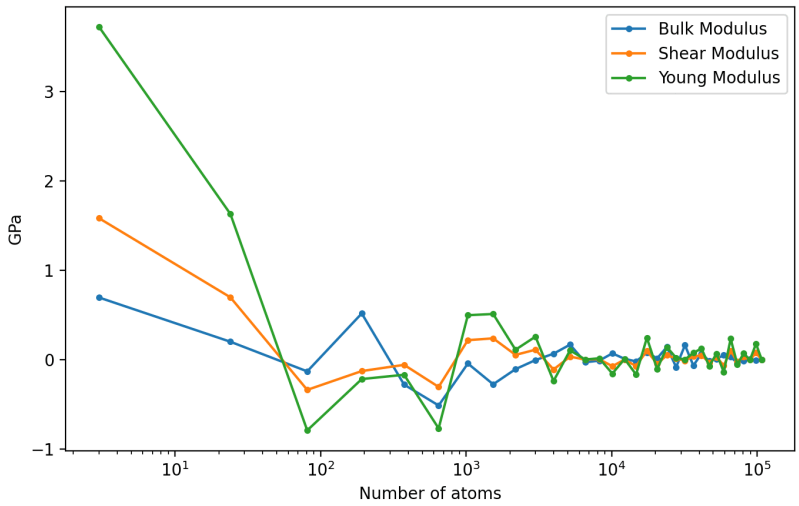

Figure 4: A simulation of the bulk Young's and shear moduli of a Zr_2Cu crystal was performed with various cell sizes ranging from a single unit cell all the way up to over 100,000 atoms. The graph shows the difference between the simulation with the highest atom count and the others. We see that the results stop depending significantly on the atom count parameter beyond the 10,000 mark. For this reason, all the simulations in this project were performed with cell sizes of around 10,000 atoms.

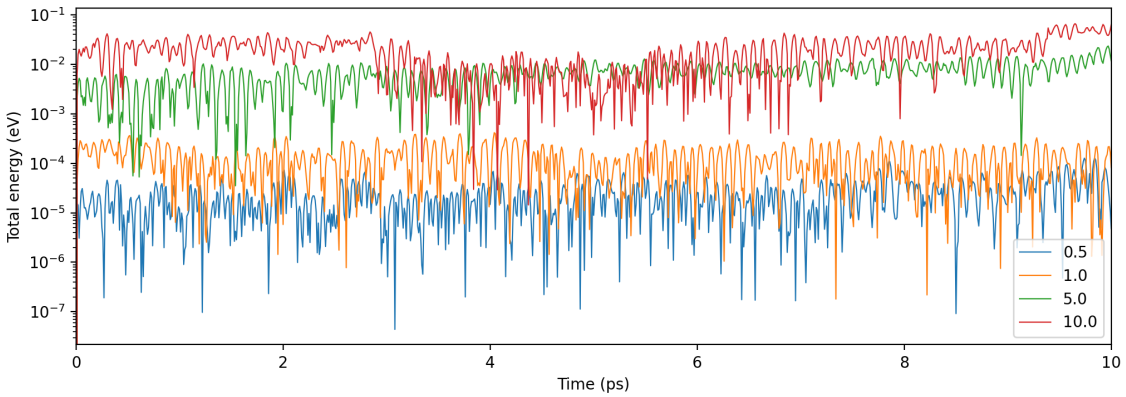

Figure 5: Energy as a function of time in multiple 10 ps long 1000 atom $CuZr2$ simulations. Different lines represent different time step durations in fs. A time step duration of 1 fs or shorter results in energy fluctuations no bigger than 10^{-3} eV, ensuring the energy is conserved over simulation times in the order of tens of picoseconds.

Not all parameters need to be set by running full simulations and comparing final results obtained with different parameter values. Often simple physical requirements of the simulation already let us determine the appropriate value of many different parameters. For example, we can obtain a maximum value for the duration of a single time step by requiring that the energy in the simulation be well conserved. In this project, the maximum length of a time step was defined by requiring that fluctuations in the total energy of a 1000-atom simulation do not exceed 0.001 eV. As shown in figure 5, the time step was determined in this way to be one femtosecond.

To make the simulations more like real melt-quench simulations, the target pressure was set to atmospheric pressure. The melting temperature, or the temperature to which the simulated alloys were heated during the melting part of the melt-quench simulation, was set to 3000 K. This temperature is well above the melting points of any of the pure phases of the constituent elements aluminium, copper, and zirconium. Furthermore, it is also far in the liquid regime of any of the Al-Cu, Al-Zr, and Cu-Zr phase diagrams, which can be found in appendix A.2.

By looking at the response to a perturbation, you can find appropriate values for the parameters controlling the strength of temperature and pressure damping. The aim is to pick parameters such that the temperature and pressure get brought back to the target value in a short enough time without introducing too large or too high frequency oscillations in the system. The response of a simulation of a $CuZr_2$ crystal structure of about 10000 atoms to a temperature perturbation of 2700 K with various values of temperature damping is shown in figure 6. A similar graph showing the response of the same system to a 5 GPa pressure perturbation is shown in figure 7. Based on these simulations, the temperature damping parameter was assigned a value of 0.1 ps, and the pressure damping was set to 5 ps.

Another important simulation parameter worth commenting on is the length of the equilibration runs in the simulations. How long every equilibration phase should last is very simulation-specific, and it must be checked that the simulation has been given enough time to equilibrate at every step after it has finished running. To make an educated guess on an appropriate equilibration time, we ran a melt quench simulation where instead of gradually changing the temperature over time, it was changed instantly from room temperature to 3000 K and back. The proposition is that the duration of any equilibration phase in the simulation must be long enough to allow the pressure and temperature to settle to their target values even after a very extreme change. Figure 8 shows that an equilibration time of 10 ps was found to be long enough to achieve these results for even the most extreme pressures and temperatures encountered in simulations.

Finally, a parameter that is of great importance for this project is the rate at which the simulated molten alloys are cooled down to form the metallic glasses. In this work this cooling rate has been set to an unrealistically high value of $2.7 * 10^{14}$ K/s to ensure minimal crystallisation would take place during the cooling. A more detailed discussion of the cooling rate can be found in a separate chapter on the subject: chapter 9.

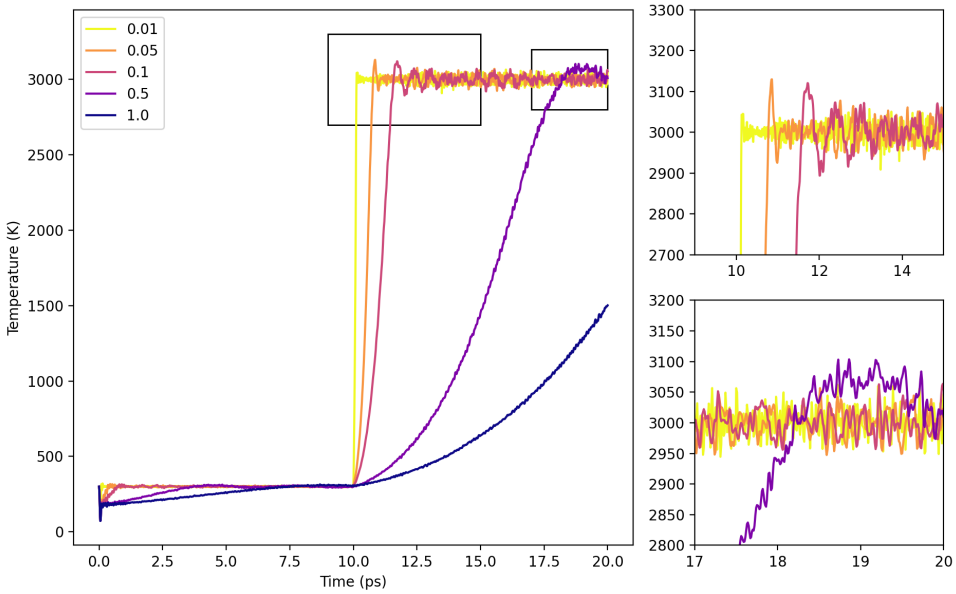

Figure 6: Temperature as a function of time in multiple 10 ps long 10000 atom $CuZr2$ simulations with a thermostat controlling the temperature. Lines correspond to varying values of the temperature damping parameter of the thermostat given in ps. After a 10 ps equilibration phase at room temperature, the temperature was increased to 3000 K to show the response of the system to large temperature perturbations. With longer temperature damping parameters of 0.5 or 1.0 ps, the simulation takes a long time to reach the target temperature. Shorter damping parameters from 0.01 to 0.1 ps have similarly sized temperature fluctuations after settling around the target temperature, as shown in the bottom right window. For these reasons, a damping parameter of 0.1 ps was used in this project for all simulations with a thermostat.

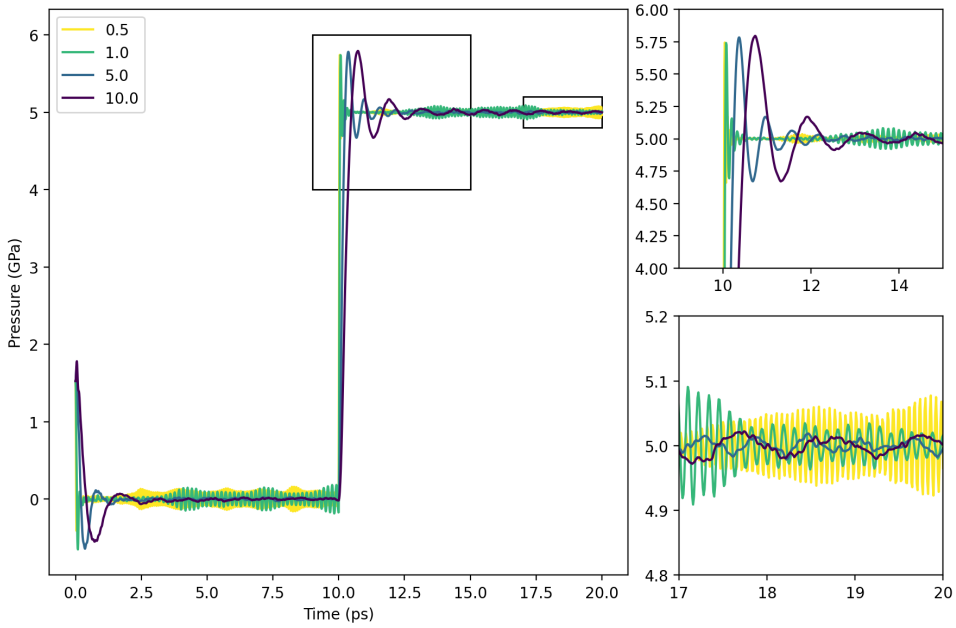

Figure 7: Pressure as a function of time in multiple 10 ps long 10000 atom $CuZr2$ simulations with a barostat controlling the pressure. Lines correspond to varying values of the pressure damping parameter of the barostat given in ps. After a 10 ps equilibration phase at atmospheric pressure, the pressure was increased by 5 GPa to show the response of the system to large pressure perturbations. With a pressure damping parameter of 10 ps, the simulation still shows strong oscillations in pressure around 5 ps after perturbing the system, as shown in the top right window. Short damping parameters of 1 or 0.5 ps result in high-frequency oscillations, as seen in the bottom right window. For these reasons, a damping parameter of 5 ps was used in this project for all simulations with a barostat.

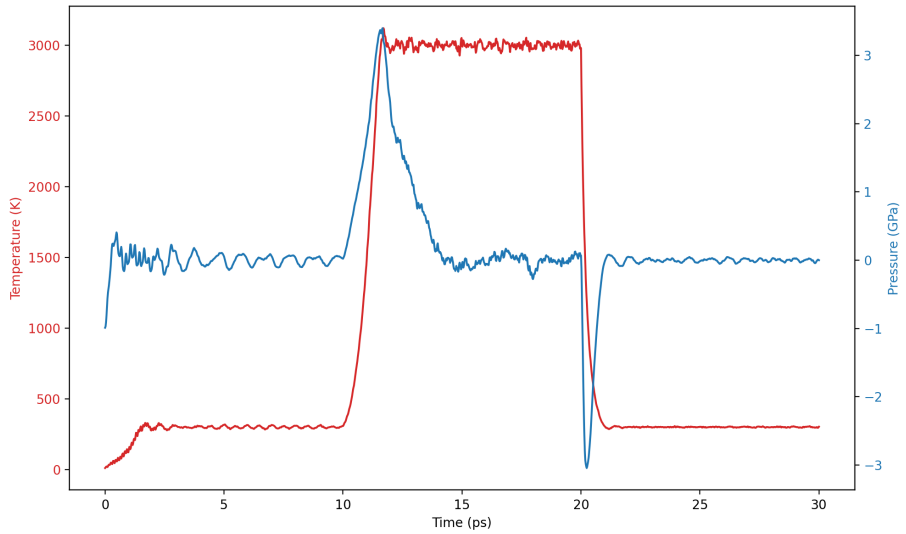

Figure 8: Temperature and pressure graphs showing a 30 ps long 10000 atom $CuZr2$ melt-quench simulation at atmospheric pressure where the target temperature is changed instantaneously from 300 to 3000 K and back after 10 and 20 ps, respectively. The figure shows that 10 ps is enough time for the temperature and pressure in the system to settle to their target values even for the most extreme heating and cooling rates.

4 Elastic Stiffness

The elastic stiffness of a material describes its resistance to deformation and is a key property for understanding mechanical behaviour. This section begins with a theoretical background on linear elasticity, introducing the stiffness tensor and its role in defining stress-strain relationships. It then discusses two methods for computing stiffness in molecular dynamics simulations: the direct deformation method, which applies small strains and measures the resulting stresses, and the stress fluctuation method, which extracts stiffness from natural stress variations in equilibrium simulations. These approaches provide a reliable way to evaluate the elastic properties of Cu-Zr-Al metallic glasses.

4.1 Linear Elasticity Theory

This section will provide some crucial background on linear elasticity theory. More specifically, we will define an object called the stiffness tensor. From this tensor, more familiar properties like the bulk, shear, or Young's modulus of a material can be derived. In section 7, we describe how these properties were used to estimate the Vickers hardness of the simulated materials.

In this section, we will outline a method to define the elastic properties of a piece of material. Formulated more precisely: we would like to know how the material responds to a deformation. A central idea here is that a deformation costs energy because the atoms are moved away from their lowest energy positions, raising the potential energy in the structure. Thus, we should aim to find some kind of stress-strain relation: a relation between the size of the deformation (strain) and the resulting change in the potential energy (stress). If we know the stress-strain relation of a hypothetical material for an arbitrary deformation, then we can say a lot about that material's elastic response.

The problem of finding a general stress-strain relation is rather challenging, if not impossible, in most cases, so some further simplifications are required. First of all, we will limit ourselves only to very small (infinitesimal) deformations. This means we are staying out of the plastic regime and only consider elastic deformations that move the atoms only slightly away from their equilibrium positions. Furthermore, we only consider a uniform deformation throughout the entire bulk of the material. We can think of this as simulating what happens to a very small piece of material if a deformation is applied slowly on a timescale far greater than the time it takes atoms to rearrange their positions. Under these two conditions, a general deformation defined by a displacement field $\vec{u}$ can be described by a constant three-by- three strain tensor ϵ_{ij} according to equation 8. The diagonal elements of the strain tensor determine the degree to which the material is stretched in each of the cardinal directions, and the off-diagonal elements determine the degree of shearing in

the xy, xz, and yz planes. The strain tensor is symmetric by definition. The stress in the system is defined by the Cauchy stress tensor σ_{ij}. Formally, it is a second-order tensor with nine components that relates any unit-length direction vector $\vec{e}$ to the traction vector $\vec{T}(\vec{e})$ across an imaginary surface perpendicular to $\vec{e}$. Under the current assumptions of a uniform material undergoing a uniform infinitesimal deformation, this Cauchy stress tensor is constant and symmetric.

$$\begin{pmatrix} \epsilon_{xx} & \epsilon_{xy} & \epsilon_{xz} \\ \epsilon_{yx} & \epsilon_{yy} & \epsilon_{yz} \\ \epsilon_{zx} & \epsilon_{zy} & \epsilon_{zz} \end{pmatrix} = \begin{pmatrix} \frac{\partial u_x}{\partial x} & \frac{1}{2}(\frac{\partial u_x}{\partial y} + \frac{\partial u_y}{\partial x}) & \frac{1}{2}(\frac{\partial u_x}{\partial z} + \frac{\partial u_z}{\partial x}) \\ \frac{1}{2}(\frac{\partial u_y}{\partial x} + \frac{\partial u_x}{\partial y}) & \frac{\partial u_y}{\partial y} & \frac{1}{2}(\frac{\partial u_y}{\partial z} + \frac{\partial u_z}{\partial y}) \\ \frac{1}{2}(\frac{\partial u_z}{\partial x} + \frac{\partial u_x}{\partial z}) & \frac{1}{2}(\frac{\partial u_z}{\partial y} + \frac{\partial u_y}{\partial z}) & \frac{\partial u_z}{\partial z} \end{pmatrix} \tag{8}$$

In the framework of linear elasticity, the stress tensor σ_{ij} and the strain tensor ϵ_{ij} are related according to the generalised Hooke's law.

$$\sigma_{ij} = C_{ijkl}\epsilon_{kl} \tag{9}$$

The object C_{ijkl} is a constant fourth-order tensor known as the stiffness tensor. A general fourth-order tensor in three dimensions has 81 components. However, the symmetry of the stress and strain tensors implies $C_{ijkl} = C_{jikl}$ and $C_{ijkl} = C_{jilk}$. These symmetries are known as the minor symmetries, and they reduce the number of independent components from 81 to 36. These 36 elements are known as the elastic constants. If the stress derives from some elastic energy potential U, then

$$\sigma_{ij} = \frac{U}{\partial \epsilon_{ij}} \Rightarrow C_{jikl} = \frac{\partial^2 U}{\partial \epsilon_{ij} \partial \epsilon_{kl}} \tag{10}$$

and since the order of differentiation is arbitrary, this implies $C_{ijkl} = C_{klij}$. These last symmetries are known as the major symmetries, and they further reduce the number of independent elastic constants from 36 down to just 21. A convenient way to write the various tensors discussed in this section is known as Voigt notation. In Voigt notation, the six independent components of a symmetric 3x3 matrix are written in a 6-dimensional vector as follows:

$$\sigma = \begin{pmatrix} \sigma_{xx} & \sigma_{xy} & \sigma_{xz} \\ & \sigma_{yy} & \sigma_{yz} \\ & & \sigma_{zz} \end{pmatrix} \tag{11}$$

$$\sigma' = (\sigma_{xx}, \sigma_{yy}, \sigma_{zz}, \sigma_{yz}, \sigma_{xz}, \sigma_{xy}) = (\sigma_1, \sigma_2, \sigma_3, \sigma_4, \sigma_5, \sigma_6) \tag{12}$$

which then enables us to write the generalised Hooke's law (equation 9) as

$$\begin{pmatrix} \sigma_1 \\ \sigma_2 \\ \sigma_3 \\ \sigma_4 \\ \sigma_5 \\ \sigma_6 \end{pmatrix} = \begin{pmatrix} C_{11} & C_{12} & C_{13} & C_{14} & C_{15} & C_{16} \\ & C_{22} & C_{23} & C_{24} & C_{25} & C_{26} \\ & & C_{33} & C_{34} & C_{35} & C_{36} \\ & & & C_{44} & C_{45} & C_{46} \\ & & & & C_{55} & C_{56} \\ & & & & & C_{66} \end{pmatrix} \begin{pmatrix} \epsilon_1 \\ \epsilon_2 \\ \epsilon_3 \\ \epsilon_4 \\ \epsilon_5 \\ \epsilon_6 \end{pmatrix} \tag{13}$$

Since the matrix is symmetric, we write only the upper triangle of C. The stiffness tensor's 21 independent components are easily readable when written in Voigt notation.

The 21 elastic constants in the stiffness tensor are not always independent; further symmetries inherent to the system can reduce the number even further. For example, if a material has a cubic crystal structure, then the additional symmetries result in only three independent elastic constants. The most symmetric case of a completely isotropic material, like metallic glass, for example, results in only two independent elastic constants, and Hooke's generalised law takes a particularly simple form.

$$\begin{pmatrix} \sigma_1 \\ \sigma_2 \\ \sigma_3 \\ \sigma_4 \\ \sigma_5 \\ \sigma_6 \end{pmatrix} = \begin{pmatrix} 2\mu+\lambda & \lambda & \lambda & 0 & 0 & 0 \\ & 2\mu+\lambda & \lambda & 0 & 0 & 0 \\ & & 2\mu+\lambda & 0 & 0 & 0 \\ & & & \mu & 0 & 0 \\ & & & & \mu & 0 \\ & & & & & \mu \end{pmatrix} \begin{pmatrix} \epsilon_1 \\ \epsilon_2 \\ \epsilon_3 \\ \epsilon_4 \\ \epsilon_5 \\ \epsilon_6 \end{pmatrix} \tag{14}$$

Where the two variables μ and λ are identified as the Lamé parameters. These are easily converted to many other familiar elastic moduli. The parameter μ is commonly referred to as the

shear modulus G. And simple formulas exist that express the bulk modulus and Young's modulus in terms of these parameters as well:

$$\text{shear modulus } G = \mu \tag{15}$$

$$\text{bulk modulus } K = \lambda + \frac{2\mu}{3} \tag{16}$$

$$\text{Young's modulus } E = \frac{9KG}{3K+G} = \frac{\mu(3\lambda+2\mu)}{\lambda+\mu} \tag{17}$$

As mentioned above, metallic glasses are isotropic materials, so their stiffness tensors take the form of equation 14, and their elastic properties are conveniently summarised in terms of bulk and shear moduli. However, in this thesis we will also compute the elastic properties of the regular crystalline phases of the alloys. Crystal structures are not isotropic, and their elastic response can not be reduced down to just two numbers like for isotropic materials. Their elastic properties depend on the direction of the deformation. For example, a crystal with a tetragonal structure might resist deformation along one axis differently from the others. Despite this, bulk and shear moduli are reported very frequently for metals of all shapes and sizes and with all types of crystal systems. That is because macroscopic pieces of metal are often polycrystalline, thus removing any directionality in the system and making the material isotropic. However, the simulations of crystalline materials performed in this project are all of pure crystals, and they typically produce stiffness tensors where all 21 elastic constants are different, like equation 13, and not like equation 14.

There are ways to estimate the bulk and shear moduli of a polycrystalline material based on the single-crystal elastic constants. In the Voigt approximation, the bulk and shear moduli are obtained from the single crystal elastic constants as follows: [9]:

$$9K_V = (C_{11} + C_{22} + C_{33}) + 2(C_{12} + C_{23} + C_{13}) \tag{18}$$

$$15G_V = (C_{11} + C_{22} + C_{33}) - (C_{12} + C_{23} + C_{13}) + 3(C_{44} + C_{55} + C_{66}) \tag{19}$$

The Voigt approximation typically overestimates the actual values of the polycrystalline elastic moduli and can be interpreted as an upper bound. In the Reuss approximation, the polycrystalline bulk and shear moduli are expressed as [9]

$$1/K_R = (S_{11} + S_{22} + S_{33}) + 2(S_{12} + S_{23} + S_{13}) \tag{20}$$

$$15/G_R = 4(S_{11} + S_{22} + S_{33}) - 4(S_{12} + S_{23} + S_{13}) + 3(S_{44} + S_{55} + S_{66}) \tag{21}$$

where the compliance tensor S is defined as the inverse of the stiffness tensor C ($S_{ij} = C_{ij}^{-1}$). Contrary to the Voigt averaging scheme, the Reuss average tends to underestimate the polycrystalline elastic moduli and can be taken as a lower bound on these values. The average of the Voigt and Reuss is known as the Voigt-Reuss-Hill (VRH) average and is known to represent the bulk and shear modulus of polycrystalline materials with comparable accuracy as more advanced methods of estimating the polycrystalline elastic moduli [9]. In this text, all bulk and shear moduli reported are computed from stiffness tensors using the VRH approximation.

4.2 Computing Stiffness

Computing mechanical properties of a system in a molecular dynamics simulation can be a challenging task. Two methods for computing the components of the elastic stiffness tensor were used in this project. The different methods and their advantages and disadvantages are discussed in the section below. The results of both of these methods will be discussed in chapter 6. We refer back to the theory section 4.1 for the theoretical underpinning of these methods and for a more in-depth discussion of these methods, see also the paper by Clavier et al. [8].

4.2.1 Direct Deformation Method

Perhaps the most straightforward and easily understandable of the two methods presented here, this method relies on directly deforming the simulation box and recording the effect this has on the stress in the system. By picking various deformations, all stress and strain relations can be obtained, and the full elastic stiffness tensor is computed.

Deformations can be picked in such a way that only a single element of the strain tensor is non-zero. Each element of the strain tensor corresponds to a unique deformation: the on-axis elements correspond to stretching in each of the cardinal x, y, or z directions, and the off-axis elements correspond to three different shearing deformations. Having only a single non-zero element in the strain tensor greatly simplifies the generalised Hooke's law. The six components of the stress tensor now grow linearly with the magnitude of the strain through six proportionality coefficients, which are exactly elements of the elastic stiffness tensor C. You can get all 36 parts of the elastic stiffness by deforming the structure six times and then recording the stress tensor's six parts after the structure has had time to relax.

This method provides a simple and elegant way to determine the elastic stiffness tensor. It does, however, introduce a number of extra simulation parameters, like the amount of simulation box deformation and the time the structure is given to relax after deforming. The method will not produce consistent and accurate results without careful adjustment of these parameters, and it is generally not computationally efficient, as it requires at least six separate structure relaxation simulations..

4.2.2 Stress Fluctuation Method

In many cases the elastic stiffness tensor can also be related to spontaneous fluctuations of some observable in the system. For example, in constant volume and temperature simulations, it is possible to relate the elastic stiffness tensor with stress tensor fluctuations. We adopt this approach here, which we will refer to as the stress fluctuation method. The stress fluctuation method introduces far less sensitive simulation parameters and is generally quicker to converge than the direct deformation method described in the previous section. The central equation in the stress fluctuation method is the following expression for the elastic stiffness tensor, written here in Voigt notation (for more detail and derivation of this relation, see Lutsko [29] and Clavier et al. [8]).

$$C_{i,j} = \left\langle C^B_{i,j} \right\rangle - \frac{V}{k_B T}\left(\left\langle \sigma^B_i \sigma^B_j \right\rangle - \left\langle \sigma^B_i \right\rangle \left\langle \sigma^B_j \right\rangle\right) + \frac{N k_B T}{V}\left(\delta_{i,j} + (\delta_{1,i} + \delta_{2,i} + \delta_{3,i}) * (\delta_{1,j} + \delta_{2,j} + \delta_{3,j})\right) \tag{22}$$

The quantities $C^B_{i,j}$ and σ^B_i are the Born contributions to the elastic stiffness tensor and the stress tensor, respectively. Together they capture the relevant information about the spontaneous fluctuations in the stress tensor. Their components are the first and second order derivatives of the potential energy in the system with respect to the strain tensor:

$$C^B_{i,j} = \frac{1}{V}\frac{\partial^2 U}{\partial \epsilon_i \partial \epsilon_j} \tag{23}$$

$$\sigma^B_i = \frac{1}{V}\frac{\partial U}{\partial \epsilon_i} \tag{24}$$

During the simulation, these Born contributions are recorded and averaged. The 36 parts of the expression in equation 22 will have converged after a long enough simulation run, and the elastic stiffness tensor will be found.

The method described above relates stress fluctuations in the canonical (NVT) ensemble to the elastic stiffness tensor. It is important to note that similar relations exist in many other ensembles. For example, strain fluctuations in the isothermal–isostress (NσT) and isothermal–isobaric (NpT) ensembles can also be used to compute the elastic stiffness tensor. The (NVT) stress fluctuation method used in this project was the only one implemented as previous research [8] has shown that the strain fluctuation methods take significantly longer to converge to the same accuracy as the NVT stress fluctuation method.

5 Radial Distribution Functions

This project primarily focusses on the impact of a disordered atomic structure on the properties of metal alloys. Since alloys are typically neither perfectly crystalline nor completely disordered, it is crucial to obtain a sense of just how disordered any given arrangement of atoms really is. The radial distribution function is a tool to do just this.

The radial distribution function (RDF) describes the probability of finding an atom a certain distance away from some reference atom. More precisely, a radial distribution function g(r) is the probability, given some random reference atom, of finding another atom a distance r away from that reference atom, divided by that same probability but for an ideal gas of the same density. In a perfect crystal structure, only very specific interatomic distances exist. As a result, the RDF of such a crystal has extremely tall, sharp peaks at these distances while it is zero everywhere else. In a very disordered amorphous material, the positions of atoms quickly become uncorrelated, and as a result, the RDF will tend towards one rapidly, which is very different from the crystal case. Thus, the RDF is sensitive to the degree of disorder present in an atomic structure.

If there are multiple element species present in the simulation, one can choose to only compute the radial distribution functions of specific elements with respect to others. These 'partial' radial distribution functions only show a subset of the peaks one would expect to find in the 'full' radial distribution function. Occasionally the structure, or lack thereof, is more easily visible in the partial radial distribution function of specific elements than it is in the full radial distribution function.

In every simulation performed for this project, the partial radial distribution functions of all nine possible combinations of Al, Cu, and Zr were computed at 0.1 ps (100 time steps) intervals throughout the simulation. The RDFs were computed up to a distance of 15 Å from the central atom. A visualization of the RDFs generated this way for a 50 ps long melt-quench simulation of a Al_5Cu_7Zr crystal is shown in figure 9. The simulation started with a 10 ps long first equilibration phase at a constant temperature of 300 K. After that the temperature is increased to 3000 K in 10 ps, kept at 3000 K for 10 ps, and then cooled back down to 300 K in 10 ps. Finally, a last 10 ps equilibration phase follows. The evolution of the simulation temperature as a function of time is shown in figure 3. Already in these figures, it is clear that the longer-range peaks present in the crystal structure rapidly disappear as soon as the temperature is increased and do not return when the structure is cooled back down and returns to a solid at room temperature.

After the simulations finished running, the radial distribution functions at the end of the first equilibration phase were compared to those of the last equilibration phase. This was done by averaging all RDFs of the last 5 ps of each respective equilibration phase to generate two sets of RDFs. In the first equilibration phase, after the crystal has been initialised and given time to relax, one would expect those RDFs to show a high degree of order in the structure in the form of sharp peaks that are present throughout the length of the graph. During the last phase of equilibration, after the crystal had been melted and then quickly cooled down, it should have had a fully amorphous structure. In this case, the RDF would not have any long-range peaks.

Figures 10 and 11 show examples of these comparisons. They show simulations of a $CuZr_2$ crystal and a Al_5Cu_7Zr crystal, respectively. Some short-range order still remains in the alloys after the melt-quench, but at distances over 10 Ångström from a reference atom, the RDFs are flat, indicating that atom positions over these distances have become almost entirely uncorrelated. This is in stark contrast with the RDF graphs of the alloys before, which all show the characteristic peaks indicating the presence of longer-range order present in the structure. The results indicate that the alloy structures, which are initially crystalline in nature, become almost completely amorphous after undergoing the simulated melt-quench steps.

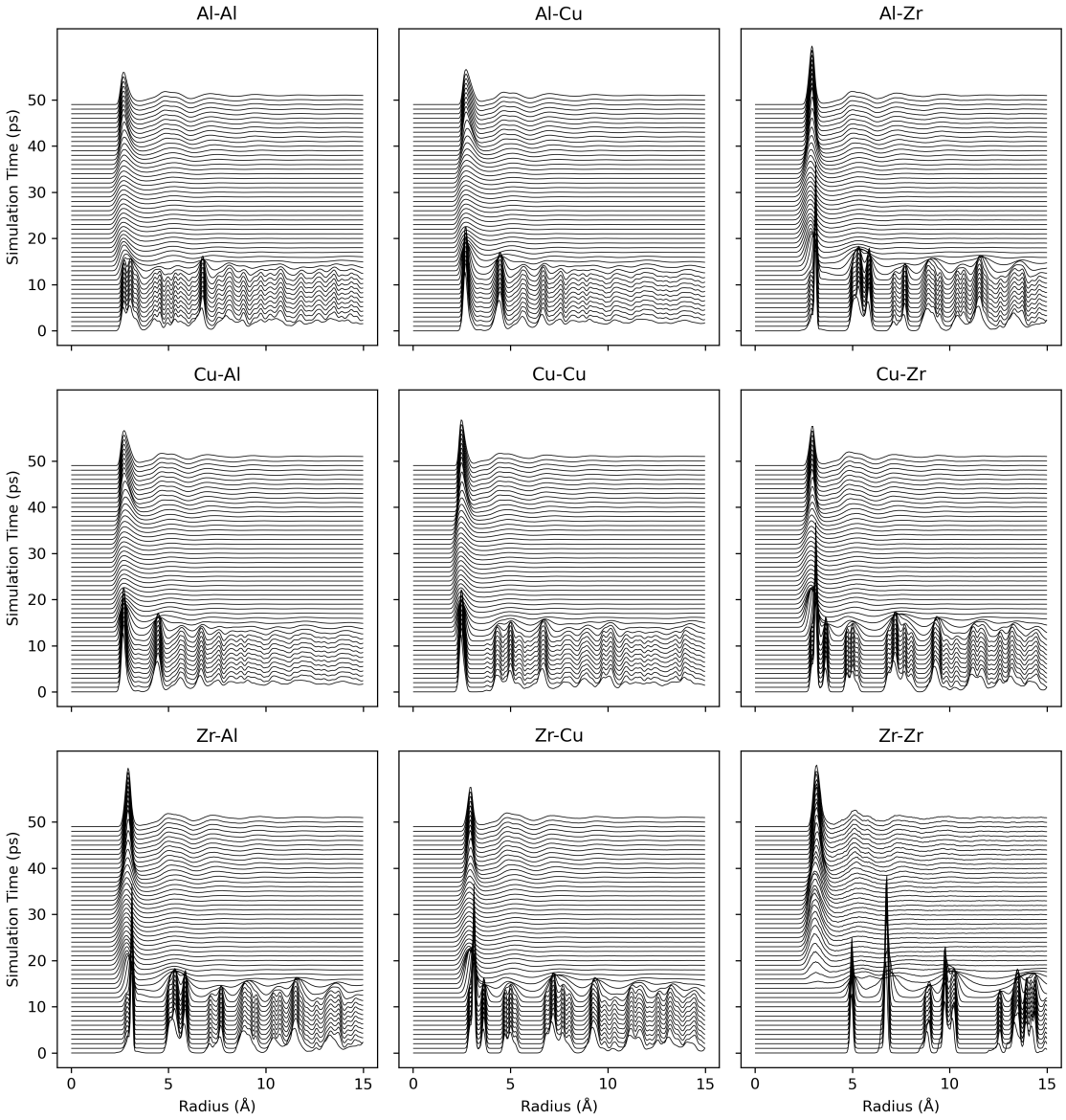

Figure 9: Partial radial distribution functions of all nine element combinations drawn at various moments in time. The simulation is of a Al_5Cu_7Zr crystal being molten and rapidly cooled back down. Total simulation runtime was 9 ps. Between 1 ps and 2 ps, the temperature was increased linearly from 300 K to 3000 K. Between 3 ps and 4 ps, the temperature was decreased linearly from 3000 K back down to 300 K. Each graphed line here is the average of 10 radial distribution functions that were taken 0.1 ps apart. In each sub-figure, the bottom line represents the start of the simulation, and the top line is the end of the simulation. The x-axis shows the distance to a central atom in Ångström.

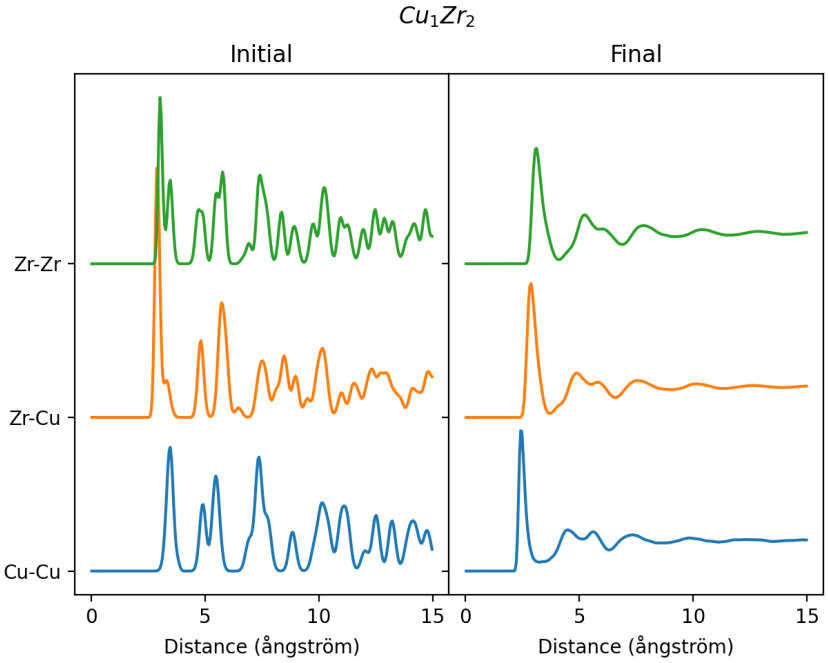

Figure 10: Comparison of the various radial distribution functions in the $CuZr_2$ crystal structure before and after the melt quench procedure. The long-range order that was present before melt-quench has disappeared in the resulting final structure, indicating the system underwent a transition from a crystalline to an amorphous structure. The RDFs shown here are time-averaged over the last five ps of the initial and final equilibration runs of the simulation.

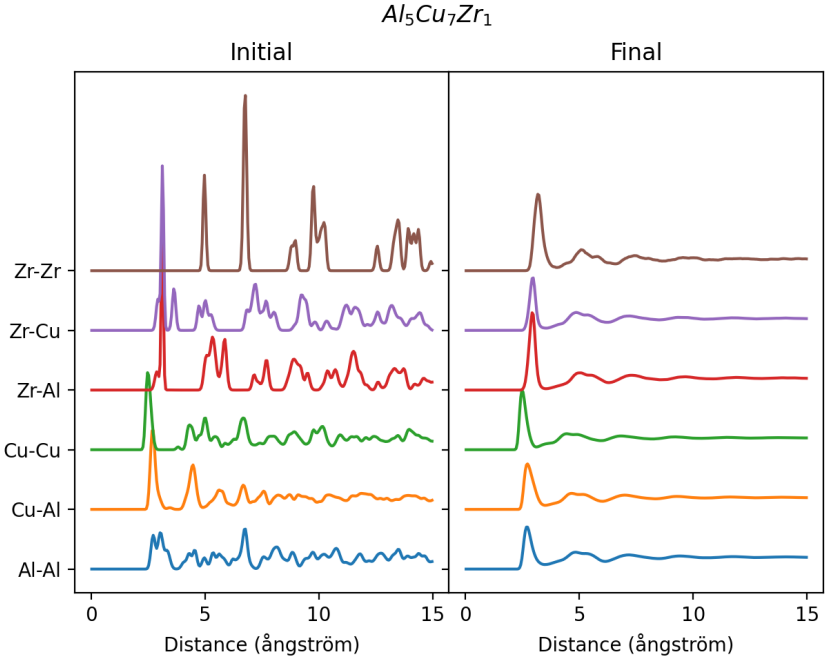

Figure 11: Plot similar to figure 10 but for the Al_5Cu_7Zr structure whose RDFs time evolution is visualised in figure 9.

6 Elastic Moduli of the Cu-Zr-Al Alloys

As discussed in chapter 4 we computed the bulk, shear, and Young's moduli of a set of alloys in the Cu-Zr binary system. These elastic moduli were computed from an elastic stiffness tensor using the Voigt-Reuss-Hill approximation. The elastic stiffness tensors needed for this were determined using both methods, the direct deformation method and the stress fluctuation method. We determined the elastic moduli of the Cu-Zr alloys both before and after the melt-quench simulation, which correspond to a polycrystalline and an amorphous phase, respectively. The results of these calculations are shown in figure 12 along with a number of literature values for the same structures.

We derived the literature values from seven distinct papers, identified by a set of shorthand names in the figures. The 'Du14' shorthand name refers to a first principles calculation study where density functional theory simulations were used to compute directly the elastic stiffness tensors of a number of crystal structures in the Cu-Zr system [10]. The same Voigt-Reuss-Hill method that was talked about in section 4.1 was used to turn these elastic constants into bulk, shear, and Young's moduli. We also include the results of two direct measurements of the stress-strain relationships of a B2 $CuZr$ crystal and a $Cu_{51}Zr_{14}$ crystal. These are called "Pauly09" and "Zhao18," respectively, in this paper. Lastly, for the crystal structures, we also include the bulk, shear, and Young's moduli of pure aluminium, copper, and zirconium metals. These pure metal values were taken from the paper referred to by the shorthand 'Yu08' [49]. That same paper also has stress-strain measurements of a number of BMGs in the $(CuZr)_{(100-x)\%}Al_{x\%}$ system including a $Cu_{50\%}Zr_{50\%}$ BMG [49]. The papers "Mattern09", "Duan08", and "Park08" all talk about the elasticity of the $Cu_{50\%}Zr_{50\%}$ BMG based on direct stress-strain measurements [31], [11], and [37]. Additionally, these papers also provide values for $Cu_{65\%}Zr_{35\%}$ [31] [37], $Cu_{64\%}Zr_{36\%}$ [11], and $Cu_{57\%}Zr_{43\%}$ [37] BMGs.

Figure 12 demonstrates that the agreement between the computed values and literature data is generally poor. However, the results do exhibit a discernible overall trend. Specifically, the computed bulk modulus values closely follow the literature values but are consistently shifted downward by approximately 10–20 GPa, indicating a systematic deviation that, while significant, is not entirely unreasonable. Similarly, the computed shear modulus values are generally within 10–20 GPa of the literature values, though they show less consistency, sometimes exceeding and at other times falling below the expected values by this margin. Based on these observations, we conclude that the methods employed in this thesis are most appropriate for providing a qualitative description of the elastic behavior of metallic glasses rather than yielding precise numerical predictions for the fundamental elastic properties of alloys in the Cu-Zr system. The Cu-Zr simulations presented in this chapter were extended to a series of crystalline structures in the Al-Cu and Al-Zr systems. At present, however, there is very little experimental data on the elastic properties of the crystals and glasses in these systems. For completeness, the corresponding results are provided in section A.1 of the appendix in figures 24 and 25.

Figure 12 allows for easy comparison of the two different methods for computing the elastic stiffness tensor that were discussed in section 4.2. Interestingly, the two methods generally agree well for the polycrystalline structures but give different results for the metallic glasses. This is especially true for the shear moduli of the metallic glasses, where the two methods consistently differ by around 15 GPa, which is then reflected also in a large discrepancy in the Young's moduli (which is computed directly from the bulk and shear moduli). Looking at the reference values, it appears that the direct deformation method is prone to overestimating the shear modulus, while the stress fluctuation method is prone to underestimating the shear modulus of metallic glasses.

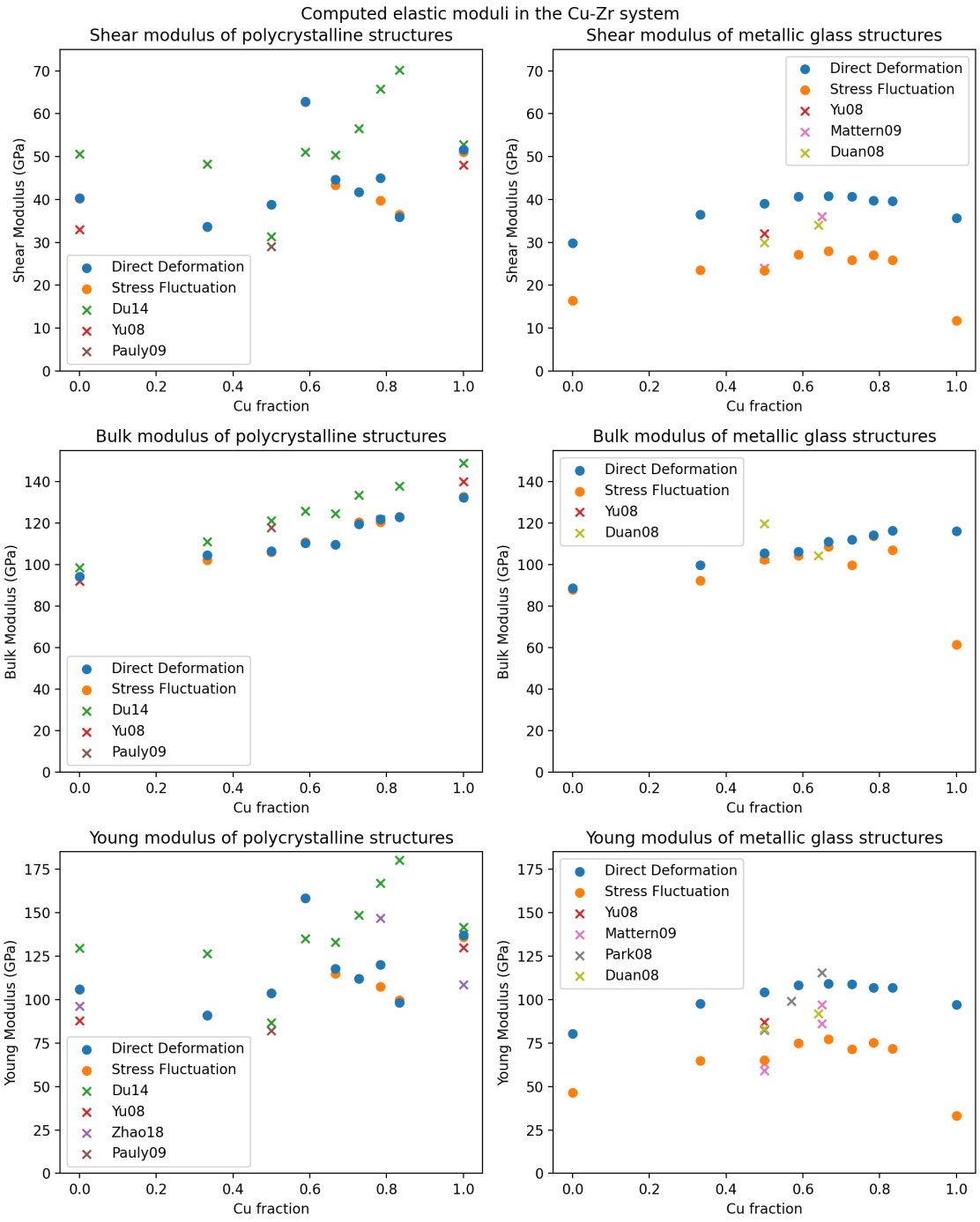

Figure 12: Bulk, shear, and Young's modulus in GPa of a number of alloys in the Cu-Zr system, both in a polycrystalline and a metallic glass phase, plotted as a function of the percentage of copper atoms. Results obtained using the direct deformation method are shown in blue, and results obtained using the stress fluctuation method are shown in orange. Also plotted are a number of values obtained from literature for these same structures. The relevant references are Du14 [10], Yu08 [49], Pauly09 [38], Zhao18 [51], Mattern09 [31], Duan08 [11], and Park08 [37]. The chemical formulae of the crystal structures are (from left to right) Zr, $CuZr_2$, $CuZr$, $Cu_{10}Zr_7$, Cu_2Zr, Cu_8Zr_3, $Cu_{51}Zr_{14}$, Cu_5Zr, and Cu.

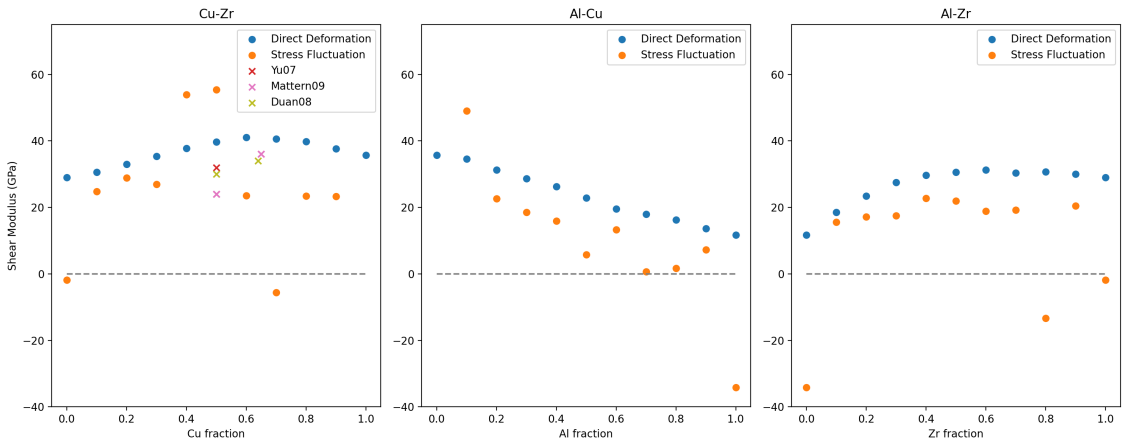

Figure 13: Shear moduli in GPa of a large range of metallic glasses in the Cu-Zr, Al-Cu, and Al-Zr binary alloy systems as a function of element fraction. Shear moduli were computed using the direct deformation and stress fluctuation methods. Structures generated using the randomised initialisation method.

As shown in figure 12, the direct deformation and stress fluctuation methods have the greatest disagreement when computing metallic glass shear moduli. To gain more insight into the difference between the two methods, we performed a large number of extra metallic glass simulations and computed the shear moduli. Simulations were performed for $A_{(100-x)\%}B_{x\%}$ structures where A and B are combinations of Al, Cu, or Zr and with x ranging from 0 to 100 in increments of 10. These metallic glass structures were all generated using the randomised initialisation method described in the 'initialisation' section of chapter 2. The outcomes of these simulations are plotted in figure 13. Here the stress fluctuation method performed significantly worse than the direct deformation method. It produced unphysical negative values for the shear moduli of structures in the Cu-Zr and Al-Zr systems as well as near-zero values in the Al-Cu system. Furthermore, the predicted shear modulus of the $Cu_{50\%}Zr_{50\%}$ metallic glass more than doubled compared to the earlier computation seen in figure 12, showing the results are also widely inconsistent.

One likely explanation for the underperformance of the stress fluctuation method is the complexity of the interaction potentials used in this study. Specifically, the derivatives of the stress with respect to strain, which are required for this method, had to be computed numerically due to the lack of an analytic solution, introducing numerical inaccuracies that may compromise the reliability of the results. Another possible explanation is that the stress fluctuation method, while generally considered reliable, may be inherently more convoluted and sensitive to simulation noise compared to the direct deformation approach, especially when applied to highly disordered systems such as metallic glasses. Additionally, it is plausible that the high degree of atomic-scale disorder in these materials exacerbates the statistical errors inherent in fluctuation-based methods, further undermining their accuracy. Because of these factors, it was decided that the hardness calculations in the next chapter, which are based on the calculated shear and bulk moduli, would only use the direct deformation method results.

7 Hardness Predictions

7.1 Binary Systems

At this point in the thesis, we have shown that we can generate metallic glass structures in the Al-Cu-Zr system and predict their basic elastic properties like bulk, shear, and Young's moduli. However, what we are really interested in from a material design perspective is the materials' hardness. Hardness is typically understood to refer to a material's ability to resist local plastic deformations like a scratch or an indentation. There are multiple different measures of hardness that are commonly in use. The basic principle of these hardness tests is to measure experimentally a material's response to a standardised source of plastic deformation. In the Vickers hardness test, for example, a pyramid-shaped diamond with exactly defined proportions is indented at a right angle to the surface, and the hardness is determined as the ratio F/A between the applied force F and the area of the resulting indentation A. Material hardness is very much an experimental quantity; it is determined with real-world experiments on actual samples. A formal mathematical definition cannot be given, as it generally depends in complex ways on many properties, such as stiffness, plasticity, viscosity, toughness, ductility, and more. This poses a challenge when trying to predict a material's hardness based solely on theoretical simulations.

How to bridge the gap between theory and experiment to be able to obtain hardness values from nothing but a simulation? What we need is a calculable figure that correlates well with a material's hardness. In 1998, David M. Teter showed the existence of a linear correlation between materials' hardness and their shear modulus over a large range of different materials [44]. Unlike hardness, the shear modulus has a precise definition, and we can obtain it from the stiffness measurements as discussed in chapter 4. Thus, the shear modulus is a calculable figure that we can use to predict the hardness of the materials simulated in this thesis.

More recently in 2011, Chen et al. [6] further refined Teter's linear relation. The authors argue that brittle materials generally follow a linear relation of

$$H_V = 0.151G \tag{25}$$

where H_V is the Vickers hardness and G is the shear modulus. They showed that this relation holds particularly well for a large range of 37 bulk metallic glasses including two BMGs in the Cu-Zr-Al system that we are studying in this project. For this reason all the hardness predictions of BMGs in this paper are done using this simple linear relation. Besides predicting BMG hardness in this project we are also interested in the hardness of their ordinary polycrystalline counterparts. To predict the hardness of polycrystalline materials Chen et al. argue that a more complicated relation is appropriate that involves the shear modulus as well as the bulk modulus. They give the following relation for the hardness of polycrystalline materials:

$$H_V = 2\left(k^2G\right)^{0.585} - 3 \tag{26}$$

where k is the ratio between the bulk and shear modulus G/K known as the Pugh ratio. However as Tian et al. [45] pointed out a year later the -3 intercept term is without physical basis and can lead to unphysical negative values of the Vickers hardness in some cases. Tian proposes a revised formula, fitted to the same data that Chen used, without the intercept term

$$H_V = 0.92k^{1.137}G^{0.708} \tag{27}$$

and it is this form that we have used to predict the hardness of all the crystalline structures in this thesis.

Figure 14 shows the computed hardness of various Cu-Zr alloys in both their polycrystalline and metallic glass phases. As discussed above, the metallic glass structures are determined by equation 25, while the polycrystalline structures are computed according to equation 27. Both pure zirconium and pure copper have very similar hardness values in the simulated polycrystalline and metallic glass phases. However, as Chen points out [6], the model used here to predict the polycrystalline hardness may be ill-suited for pure metals and is prone to overestimating the hardness of these metals. Furthermore, it should be noted that the metallic glass phase of the pure metals Cu and Zr is strictly theoretical; as of the writing of this thesis, no pure copper or pure zirconium metallic glass structures have ever been produced in a lab, presumably because the cooling rate required to prevent crystallisation of pure metals is far higher than what can be achieved with current technology. Three of the four intermetallic compounds considered in the Cu-Zr alloy system show a significant increase in hardness going from a polycrystalline to a metallic glass structure. The data point corresponding to the polycrystalline phase of the $Cu_{10}Zr_7$ structure is a clear outlier

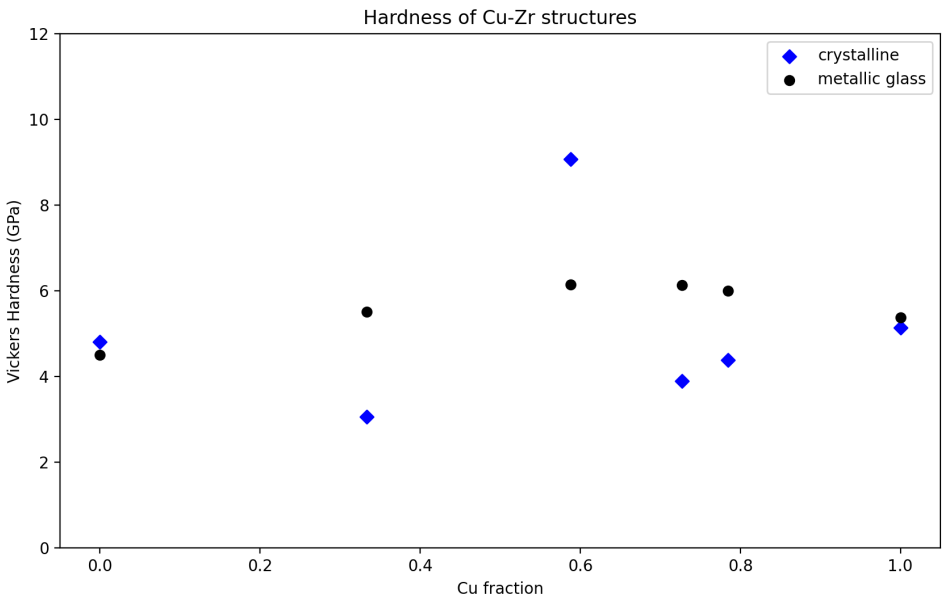

Figure 14: Vickers hardness of various alloys in the Cu-Zr system arranged by copper percentage computed from shear and bulk moduli. For each alloy, the hardness of both the crystalline and metallic glass phases was calculated. The hardness of the crystalline phases is modelled using Tian's hardness model according to equation 27, and the hardness of the metallic glass phases is modelled using Teter's linear relation as per equation 25. The chemical formulae for the structures are from left to right: Zr, $CuZr_2$, $Cu_{10}Zr_7$, Cu_8Zr_3, $Cu_{51}Zr_{14}$, and Cu.

with a predicted hardness value significantly higher than any other structures considered for this system, even surpassing the hardness of its own metallic glass phase. One potential explanation is that the $Cu_{10}Zr_7$ crystal structure has historically not been as well described in literature as other crystal structures in the Cu-Zr binary system [13]. The crystallographic database [19] used to initialise the simulations in this project only included a $Cu_{10}Zr_7$ crystal structure that was based on simulations and not experiments, potentially hurting the simulation accuracy.

Figures 15 and 16 show the computed hardness of various alloys in the Al-Cu and Al-Zr binary systems. We reiterate that the hardness model used to predict the hardness of the polycrystalline phase has a tendency to break down in the case of pure metals. Most intermetallic compounds in the Al-Cu system are harder in the metallic glass phase than they are in the polycrystalline phase, Al_2Cu_6 being the only exception. In the Al-Zr system, the effect on the material's hardness of going from a polycrystalline to a metallic glass phase is ambiguous, resulting in a decrease in hardness just as often as it results in an increase. Overall, it can be said that the hardest metallic glasses in any of the binary systems studied in this project are formed in the Cu-Zr system around a 2:1 copper to zirconium ratio. We observe a general trend where the metallic glass hardness varies far less wildly from one elemental composition to the next compared to the polycrystalline hardness results. A small increase in the fraction of one element compared to the other does not result in a large change in hardness. This is to be expected as metallic glasses are essentially purely defined by their elemental makeup and method of cooling/casting. As the latter was kept constant for all metallic glasses in this study, we should expect metallic glasses that are very close in composition to exhibit very similar material properties. On the other hand, the hardness of polycrystalline materials can depend on many intricacies of the crystal structures, and as such, crystal structures that are close in chemical composition can exhibit vastly different mechanical properties.

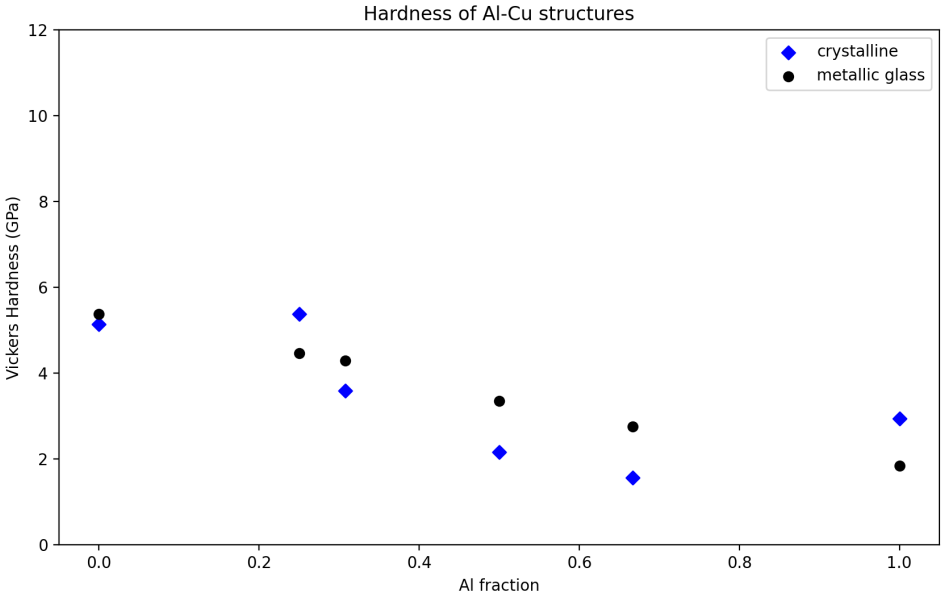

Figure 15: Vickers hardness of various alloys in the Al-Cu system arranged by copper percentage computed from shear and bulk moduli. For each alloy, the hardness of both the crystalline and metallic glass phases was calculated. The hardness of the crystalline phases is modelled using Tian's hardness model according to equation 27, and the hardness of the metallic glass phases is modelled using Teter's linear relation as per equation 25. The chemical formulae for the structures are from left to right: Cu, $AlCu_3$, Al_4Cu_9, $AlCu$, Al_2Cu, and Al.

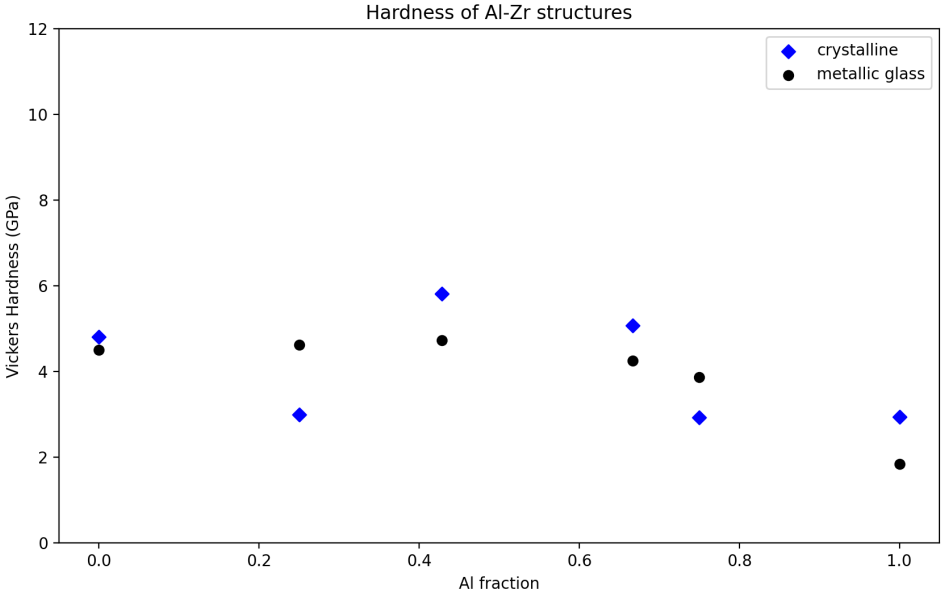

Figure 16: Vickers hardness of various alloys in the Al-Zr system arranged by copper percentage computed from shear and bulk moduli. For each alloy, the hardness of both the crystalline and metallic glass phases was calculated. The hardness of the crystalline phases is modelled using Tian's hardness model according to equation 27, and the hardness of the metallic glass phases is modelled using Teter's linear relation as per equation 25. The chemical formulae for the structures are from left to right: Zr_2, $AlZr_3$, Al_3Zr_4, Al_2Zr, Al_3Zr, and Al.

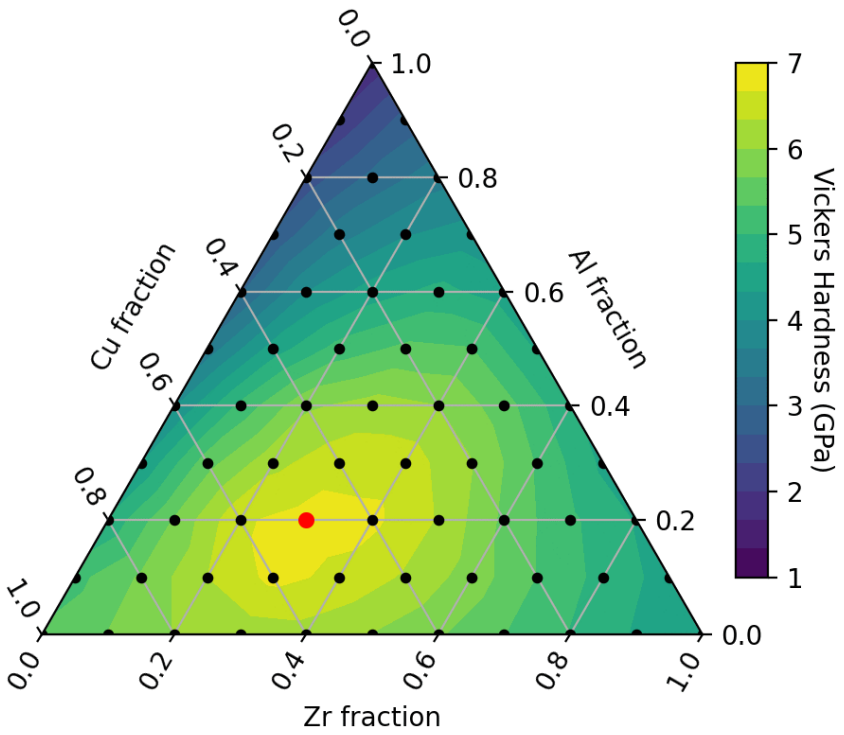

Figure 17: Vickers hardness in GPa of metallic glasses generated with a broad range of elemental compositions in the Al-Cu-Zr tertiary system. Each dot represents a different simulation. The highest predicted hardness of 6.80 GPa was found at an elemental composition of 20% aluminium, 50% copper, and 30% zirconium, and this simulation is marked by a red dot.

7.2 Tertiary System

As we stated before, one expects the material properties of metallic glasses to be almost exclusively defined by their elemental makeup and the way in which they are cast. If the method for forming them is kept constant by carefully controlling variables such as the melting temperature and the cooling rate, then the expectation is that the elemental makeup of the glass alone is responsible for any difference in material properties. We have shown the graphs 14, 15, and 16 of the three binary alloy systems, which indeed show the behaviour one would expect if this were the case. It is natural to wonder if there is a specific ratio of the three elements considered in this study that leads to a maximal expected hardness. For this purpose, 66 simulations were performed with very specific elemental compositions using the randomised initialisation method described in the 'initialisation' section of chapter 2. The elemental ratios in these metallic glasses were picked so that they would evenly cover the compositional space of all possible combinations of aluminium, copper, and zirconium. The results of these simulations have been visualised in a ternary plot in figure 17. The results suggest the hardest metallic glasses in the Al-Cu-Zr tertiary system are formed when the elemental makeup of the metallic glass is around 20% aluminium, 50% copper, and 30% zirconium. Note that we are only commenting on the predicted hardness of the metallic glass and leave open the question of whether the optimal composition presented here is in any way a good glass former. We merely claim that if it were possible to create a metallic glass with this elemental makeup, it would be harder than all other metallic glasses in the Al-Cu-Zr system.

To close out this chapter on the hardness of metallic glasses, we would like to make final remarks on the degree of uncertainty present in these results. First of all, it is important to remember that even experimentally measured hardness can vary by more than 10% for the same material [14]. Even in the best of cases, we cannot hope to do better than experiments using an almost purely theoretical approach. Basic computational limitations mean that any simulation of the macroscopic properties of a material will inevitably have to involve assumptions and approximations so that the simulation can run in a finite amount of time. While the molecular dynamics approach used in this project allows for the simulation of tens of thousands of atoms, that still means we are simulating pieces of material that are only a tenth of a micrometre across. By imposing periodic boundary conditions, we can get a sense of what a macroscopic piece of the simulated material would behave like, but there are several macroscopic effects that we can never hope to capture

in our simulations this way. The effect of grain boundaries and other large-scale impurities can have a profound impact on the mechanical properties of a material, and these are not included in the simulations performed in this project. Material hardness is usually defined as the outcome of an indentation experiment, in which case surface effects could potentially have an impact on the hardness of materials. The imposed periodic boundary conditions required for the simulations in this study ensure that no surface effects are considered at any point. Finally, on top of all the points made above, there is also the uncertainty inherent to the use of empirically fitted formulas like equations 25 and 27. Tian mentions in his paper that equation 27 has a tendency to overestimate hardness values of 'softer' materials such as the conventional polycrystalline alloys considered in this study [45].

8 Voronoi Polyhedra Analysis

Perhaps the most fundamental feature of a crystalline material is that two atoms one unit-cell spacing apart will experience exactly the same local environment. The positions and element species of the nearest neighbours and the next nearest neighbours, etc., will be perfectly identical. In an amorphous structure, all the atoms live in their own unique local environment; the material never looks exactly the same from the perspectives of two different atoms. This certainly does not mean that all local arrangements of atoms are equally likely to occur. A first step in obtaining an understanding of the typical neighbourhoods of atoms in an amorphous structure is to perform a Voronoi polyhedra analysis.

A Voronoi polyhedra analysis starts by creating a Voronoi decomposition of the entire simulation box. For each atom, there is a corresponding region, called a Voronoi polyhedron, consisting of all points of the volume closer to that atom than to any other. The atom at the centre of a polyhedron is referred to as the central atom of the polyhedron. A simple example of a Voronoi decomposition is shown in figure 18. All points that lie on the face of a Voronoi polyhedron are an equal distance away from two different atoms by definition. Thus, the faces of polyhedra can be thought of as separating two nearest neighbour atoms. In this context then, the average number of faces of the Voronoi polyhedra can be thought of much like a coordination number, indicating the amount of atoms that are next to the central atom. And the average volume of the polyhedra indicates the amount of space atoms typically take up in the structure. Voronoi diagrams can be computed efficiently during the runtime of the simulation.

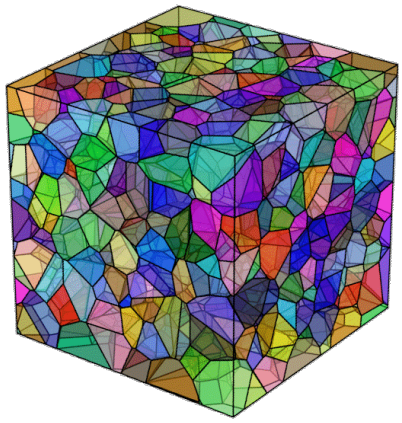

Figure 18: An example of a Voronoi decomposition of 1000 atoms with random positions inside a cube. The diagram shows the 1000 corresponding Voronoi polyhedrons with distinct colours.

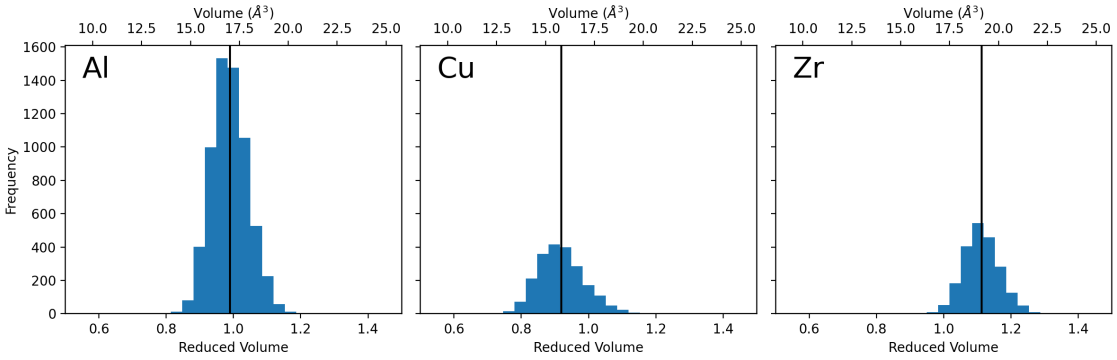

Figure 19: Distribution of the volume of polyhedra in a $Al_{20}Cu_{50}Zr_{30}$ metallic glass, separated by central atom element species with aluminium atoms on the left, copper atoms in the centre, and zirconium atoms on the right. The top axis shows the absolute volume in Å^3, while the bottom axis shows the volume normalised with respect to the average volume per atom, which in this simulation was 16.62 Å^3. The black lines indicate the mean volume for each element species.

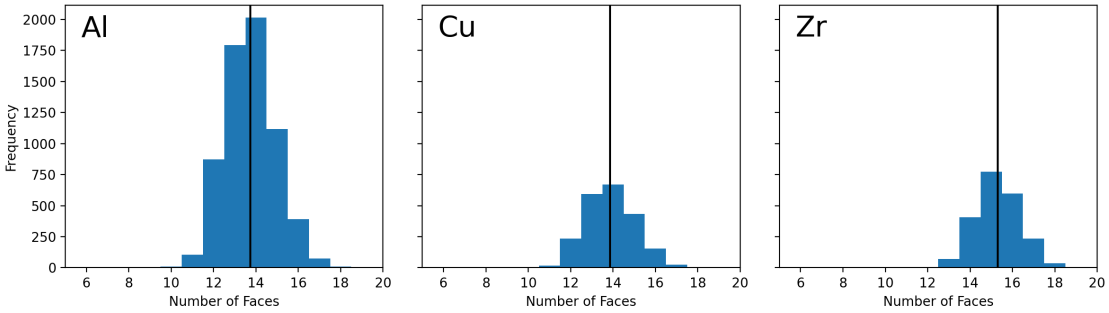

Figure 20: Distribution of the total number of faces per polyhedron in a $Al_{20}Cu_{50}Zr_{30}$ metallic glass, separated by central atom element species with aluminium atoms on the left, copper atoms in the centre, and zirconium atoms on the right. The black lines indicate the mean number of faces for each element species.

8.1 Voronoi Analysis of Al20Cu50Zr30

In section 7.2, a $Al_{20}Cu_{50}Zr_{30}$ metallic glass was predicted to have the highest hardness of any metallic glass in the Al-Cu-Zr system. The results of a single Voronoi polyhedra analysis of this same metallic glass are shown in figures 19, 20, and 21 as an example. Figure 19 shows that in this structure copper atoms take up the least amount of space on average, followed by aluminium atoms and finally zirconium atoms, which take up the most space on average. The fact that the different element species take up different amounts of space in the structure is an important feature of many metallic glasses. It is clear that the theory of metallic glass formation is very closely related to a problem of the dense random packing of unequally sized spheres. Figure 20 agrees well with the idea that the number of faces is closely related to the volume, with smaller volumes generally leading to a lower number of faces and larger volumes leading to a higher number of faces. Thus, in this metallic glass, copper atoms are generally surrounded by fewer other atoms, while zirconium atoms are surrounded by more. Figure 21 shows the number of faces split up even further not just by the element species of the central atom but also by that of the neighbouring atom. Pairings of the central atom with an aluminium atom generally occur the least, while pairings between a central atom and a copper atom occur the most. This behaviour is in line with what one would expect from a material that has far more copper atoms (50%) and far fewer aluminium atoms (20%). However, despite there being slightly more zirconium than aluminium atoms in this structure, the results in figure 21 seem to suggest Al-Zr pairs are slightly more common than Al-Cu pairs, but it is difficult to draw definite conclusions. Clearly, it can be difficult to separate the influence of the elemental makeup of a structure from the influence of any implicit preference for a certain atom pairing over another. We will come back to these issues at the end of this chapter in section 8.3, where a way to account for the influence of the elemental makeup on the frequencies of element pairs is presented.

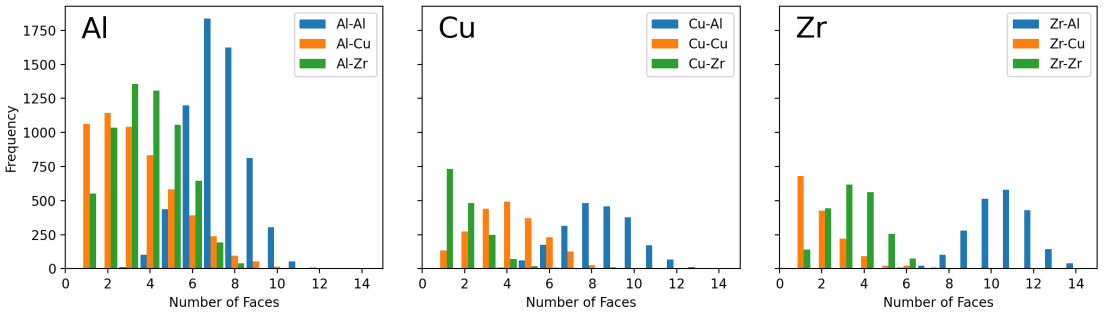

Figure 21: Distribution of the number of faces per polyhedron for each pair of elements in a $Al_{20}Cu_{50}Zr_{30}$ metallic glass, separated by central atom element species with aluminium atoms on the left, copper atoms in the centre, and zirconium atoms on the right.

8.2 Average Polyhedron Volume and Number of Faces

The analysis whose results have been shown in figures 19, 20, and 21 was repeated for all 66 of the randomly initialised structures first presented in the 7.2 section. The mean values of the polyhedron volume, area, and total number of faces, as well as the reduced volume, were recorded. The results for the alloys in the binary Cu-Zr, Al-Cu, and Al-Zr systems are shown in figure 22. The general shape of the mean polyhedron volume graphs in the top left can largely be explained by the difference in atomic volumes of the three constituent elements. These are around 10.0, 7.1, and 14.1 cm^3/mol for Al, Cu, and Zr, respectively. Thus, since a mole of zirconium takes up about twice as much space as a mole of copper, we expect the average size of the polyhedra to roughly double when going from pure copper to pure zirconium. From the atomic volumes of Al, Cu, and Zr, we expect the copper polyhedra to take up less space than the aluminium ones and for zirconium to take up more space than either. Most simulations follow this trend; however, we see that at high aluminium concentrations ($\geq$80%), some alloys in the Al-Cu system break the order, and the copper atoms take up more space instead of the aluminium. The reduced volume largely accounts for the effect of the difference in atomic volumes by dividing the absolute polyhedron volumes by the structure's average volume per atom, computed by dividing the total simulation box volume by the total number of atoms. The trends observed in the absolute volume graphs remain, however, with the ordering of Cu $<$ Al $<$ Zr only being broken in the $\geq$80% aluminium alloys of the Al-Cu system. Unsurprisingly, the area graph is nearly identical to the volume graph, illustrating that larger polyhedra generally have a bigger area while the average number of faces closely matches the trends observed in the reduced volume.

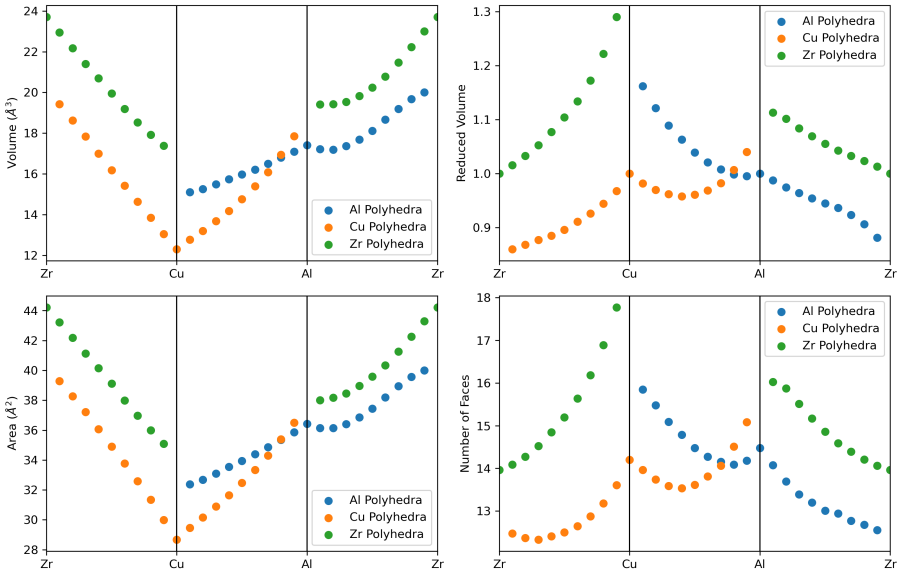

Figure 22: Results of Voronoi polyhedra analyses of various metallic glasses in the Zr-Cu, Al-Cu, and Al-Zr systems arranged along the x-axis by element fraction. All data on the Voronoi polyhedra have been separated by central atom element. Top left shows the mean volume of the polyhedra in $Å^3$. Top right shows the average reduced volume of the polyhedra where the absolute volume has been divided by the average volume per atom for that alloy. Bottom left shows the average area of the polyhedra in $Å^2$, and bottom right shows the average number of faces of the polyhedra.

8.3 Element Pair Frequencies

Finally for this chapter we will take a closer look at the distribution of the number of faces per pair of elements like in figure 21. We can use this data to make statements about how often certain elements are found next to one another. Consider, for example, a metallic glass in the binary Cu-Zr element system. If it was far more energetically favourable for Cu atoms to sit close to Zr atoms as opposed to Cu sitting next to Cu, then this could have consequences for the type of structures that are formed in the metallic glass, which could in turn influence the material properties of said glass. By counting how often elements are found next to each other, we obtain a further glimpse of what typical local neighbourhoods of atoms in our metallic glass look like. In a binary alloy system of Cu and Zr atoms, there are three possible pairs of elements: Cu-Cu, Zr-Zr, and Cu-Zr. We can look at all the pairs of atoms that share a face in the Voronoi tessellation and count how often they belong to each of the three possible element pairs. However, just counting how often each of the element pairs occurs in a glass is not enough to show a preference for a certain element's pairing over another. We would like to compare it to the number of pairs of that type we would expect to find in a structure if there is no preference for any element to sit next to any other element. We find these expected values by considering that, in the case of no element pair preferences, the percentage of pairs that are of a certain type is entirely dependent on the element fractions, as follows:

$$\begin{aligned} frac(Cu-Cu) &= frac(Cu)^2 \\ frac(Cu-Zr) &= 2 * frac(Cu) * frac(Zr) \\ frac(Zr-Zr) &= frac(Zr)^2 \end{aligned} \tag{28}$$

where frac(Cu) refers to the fraction of the total number of atoms that are copper atoms and frac(Cu-Zr) refers to the percentage of Voronoi atom pairs that consist of one copper atom next to one zirconium atom. For example, in a Zr_2Cu metallic glass where a third of the atoms are copper, we expect to find 11.1% Cu-Cu, 44.4% Cu-Zr, and 44.4% Zr-Zr pairs. Counting the atom pairs in the Voronoi tessellation of the Zr_2Cu simulation reveals that 7.59% were Cu-Cu pairs, 44.20% Cu-Zr, and 48.21% Zr-Zr. This indicates that in this alloy, Cu-Cu pairs are energetically less favourable, and Zr-Zr pairs are energetically more favourable. By repeating this same analysis for all metallic glass simulations, we can make some general statements about the preference for certain atom pairings in the Cu-Zr-Al system.

Table 2: Average percentage difference between the fraction of atom pairs of a certain element combination and the expected fractions according to equation 28. The top row contains the percentage differences averaged over all metallic glasses in the Al-Cu-Zr system, while the other rows contain averages taken over only metallic glasses in the binary Cu-Zr, Al-Zr, and Al-Cu systems.

	Al-Al	Cu-Cu	Zr-Zr	Cu-Zr	Al-Zr	Al-Cu
Al-Cu-Zr	-2.01%	-1.72%	1.19%	-0.08%	3.39%	-0.25%
Cu-Zr		-4.86%	2.32%	2.53%		
Al-Zr	-4.71%		0.08%		4.63%	
Al-Cu	-1.32%	-3.31%				4.64%

The above analysis was repeated for all 66 simulations generated using the randomised initialisation method that were discussed at the end of chapter 7. The fraction of atom pairs of a certain element combination was recorded and compared to the expected fraction according to equation 28. The percentage differences were recorded and averaged over all metallic glasses in the Al-Cu-Zr system. Averages of only the metallic glasses in the Cu-Zr system as well as those in the Al-Zr and Al-Cu systems were also recorded. The results of these analyses are shown in table 2. The results show that Al-Al and Cu-Cu pairs were found significantly less often in all systems, while Zr-Zr pairs were generally found more, albeit only very slightly in the case of the Al-Zr alloys. In all three binary systems, there was a strong preference for atoms to be adjacent to those of the other element species. However, averaged over the entire tertiary Al-Cu-Zr system, only the Al-Zr pairs are found more often. This confirms the suspicion gained back in section 8.1 from looking at figure 21 that there is a general preference for Al-Zr pairs to form in the Al-Cu-Zr system.

Table 3: Critical cooling rates for a number of metallic glasses. Data taken from reference [41].

Metallic Glass	Critical Cooling Rate (K/s)
$Au_{55}Cu_{25}Si_{20}$	$3.4 * 10^4$
$Fe_{48}Cr_{15}Mo_{14}Y_2C_{15}B_6$	$140 - 190$
$Co_{75}Si_{15}B_{10}$	$3.8 * 10^8$
$Fe_{79}Si_{10}B_{11}$	$3.7 * 10^8$
$Ni_{75}Si_8B_{17}$	$2.4 * 10^8$
$Pd_{77.5}Cu_6Si_{16.5}$	$1.5 * 10^8$
$Pd_{40}Ni_{40}P_{20}$	$1.4 * 10^7$
$Zr_{41.2}Ti_{13.8}Cu_{12.5}Ni_{10.0}Be_{22.5}$	≤ 10
$Al_{51}Ge_{35}Ni_{14}$	10^4
$Fe_{76}Si_9B_{10}P_5$	≤ 550
$Pd_{40}Cu_{30}Ni_{10}P_{20}$	$2.08 * 10^{-5}$
$Au_{49}Ag_{5.5}Pd_{2.3}Cu_{26.9}Si_{16.3}$	600
$Zr_{52.5}Ti_5Al_{10}Ni_{14.6}Cu_{17.9}$	$10^3 - 10^5$
$Fe_{67}Mo_{4.5}Cr_{2.3}Al_2Si_3C_7P_{8.7}B_{5.5}$	$9.3 * 10^4$
$Al_{86}Ni_6Y_{4.5}Co_2La_{1.5}$	$3.01 * 10^3$

9 On the Effect of Cooling Rate

An important simulation parameter that has so far hardly been discussed is the rate at which the alloys are cooled down from their molten state back down to room temperature in the simulations. The cooling rate, typically measured in K/s, with which an alloy was formed can have a profound impact on the material properties. At one extreme, an incredibly high cooling rate leads to the formation of a fully amorphous structure known as metallic glass, thanks to the crystallisation not being given enough time to take effect. At the other extreme, a cooling rate close to zero results in the formation of a fully crystalline material instead. In between these two extremes, materials could crystallise only partially, forming structures that are neither fully amorphous nor fully crystalline. Thus, fine control of the cooling rate could allow for the creation of all kinds of intermediate materials that are in between the two extremes of a metallic glass and a fully crystalline material.

The minimum cooling rate required to cast a fully amorphous ingot is known as the critical cooling rate of a metallic glass. All metallic glasses have a critical cooling rate. When a molten alloy is cooled down more rapidly than this critical cooling rate, it will result in the formation of a metallic glass. Together with the size of the ingot being formed, it dictates the glass-forming ability, or GFA, of a metallic glass. The GFA of a metallic glass heavily influences the ease with which components made of said metallic glass can be produced and is therefore an important property of metallic glasses. By simulating metallic glasses at various cooling rates and determining whether or not crystallisation has taken place, one could in theory predict the critical cooling rate of a metallic glass through simulation. This thought has led to the main question posed in this chapter: Would it be possible to use the molecular dynamics simulation method developed in this thesis to study not only the hardness but also the glass-forming ability of metallic glasses by determining the critical cooling rate?

In order to accurately numerically solve the equations of motion, the time in a molecular dynamics simulation needs to be discretised in small time steps. In section 3.3, the maximum length of such a time step was determined to be one femtosecond. The computing cost of a simulation is directly proportional to the number of time steps it takes; therefore, MD simulations typically do not cover a large amount of real-time. In the 50 ps long simulations in this work, the cooling rate has been set to the highest rate that the thermostat and barostat could keep up with. As a result, during the cooling step the temperature is brought down from 3000 K to 300 K in only 10 ps which equates to a cooling rate as high as $2.7 * 10^{14}$ K/s. As table 3 clearly shows, metallic glasses can have vastly different critical cooling rates, but the aforementioned cooling rate of the simulations in this thesis is many orders of magnitude higher than all of them.

That is why here we present an investigation into the effect of lowering the cooling rate in the simulations. For this purpose, we have repeatedly halved the cooling rate of a $CuZr_2$ simulation down to a cooling rate of around $5.3 * 10^{11}$, 512 times lower than the cooling rate of the original simulations in the rest of this study. The main tools used in this investigation are the radial distribution functions, since they are especially sensitive to the amount of crystallisation that took place. The results of these simulations are shown on the left side of figure 23. The figure shows only

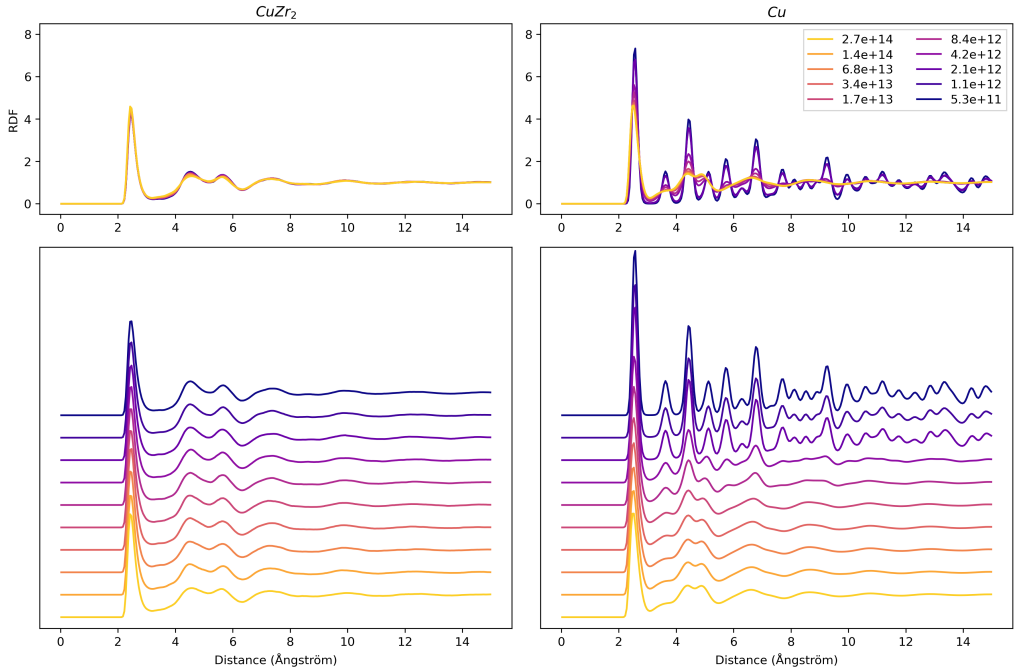

Figure 23: Radial distribution functions of metallic glass simulations with varying cooling rates during the quench step of the simulation. A metallic glass made of $CuZr_2$ is shown on the left, and one made of Cu is shown on the right. In the top figures, the various RDFs are drawn on top of one another, and in the bottom figures, the same RDFs are drawn side by side. The highest cooling rate simulations are the same simulations that have been discussed in earlier chapters. The other RDFs come from simulations with a quench step that took up to 512 times as many time steps as the original simulations, resulting in a 512 times lower cooling rate.

a very subtle sharpening of the peaks in the RDF and no emergence of the peaks at longer ranges that are indicative of crystal structure. This suggests the atoms have perhaps rearranged ever so slightly towards a more crystalline structure, but overall the material is certainly still amorphous. We conclude that the cooling rate used in these simulations, even when reduced by a factor of over 500, is still far too high to capture the crystallisation that is expected to occur on longer timescales.

The fact that no crystallisation of the $CuZr_2$ structure was observed is perhaps not surprising, seeing as the lowest cooling rate is still many orders of magnitude larger than typical critical cooling rates for metallic glasses. That is why the same analysis was also repeated for an alloy that crystallises more easily. Pure metals are known to have poor glass-forming ability, and thus their critical cooling rate is typically far higher than the critical cooling rates of excellent glass formers like $CuZr_2$. That's why pure copper was picked for this purpose. The radial distribution functions at various cooling rates of pure copper are shown next to those of the $CuZr_2$ simulations on the right of figure 23. In these figures, there is a clear emergence of longer-range peaks at the lower cooling rates, which show significant crystallisation. The RDFs show a drastic change in the long-range order as the cooling rate decreases from $4.2 * 10^{12}$ to $2.1 * 10^{12}$ K/s, indicating that the critical cooling rate of pure copper lies in this range.

We conclude that in its current form, the molecular dynamics simulation method, as developed in this project, can only determine the critical cooling rate of metallic glass materials that have an extremely low glass-forming ability, like pure copper. Typically, the simulations don't achieve cooling rates low enough for crystallization to be observed in good glass forming metallic glasses. However, the detection of crystallisation in the pure copper sample suggests that with a technique similar to this one, some metallic glass's critical cooling rates could be determined. It should be noted that all simulations in this project start by heating the alloy to a temperature of 3000 K. As the phase diagram in appendix A.2 shows, this is significantly higher than the typical melting points of alloys in the Cu-Zr system. Lowering the starting temperature to just above the melting point and raising the final temperature to just below the freezing point is one way to allow for the simulations to reach lower cooling rates. Other measures, like decreasing the number of atoms included in the simulation, could help lower computation costs, making it feasible to simulate at even lower cooling rates.

10 Conclusion

The central question of this research was whether the hardness of a material always improves when transitioning from a polycrystalline structure to its metallic glass phase. Our findings demonstrate that this is not universally the case. While metallic glasses often exhibit enhanced hardness, this improvement is not consistent across all alloys. Determining the elemental composition that would yield the hardest metallic glass revealed that the hardness of metallic glasses is not merely a simple weighted average of the hardness of their constituent elements. But that in metallic glasses the sum can be greater than its parts and metallic glasses can be significantly harder than any of the metals they are made of.

The methodology of this project relied on molecular dynamics simulations to investigate the mechanical properties of metallic glasses in the Al-Cu-Zr system. It involved initialising crystal structures, performing melt-quench simulations to generate amorphous phases, and subsequently analysing their elastic and hardening properties. Molecular dynamics offered significant advantages, including the ability to efficiently explore a wide range of alloy compositions and simulate processes on a scale that would be time-consuming or prohibitively expensive in experimental settings. However, the method also has its limitations. The accuracy of the results is heavily dependent on the quality of the interatomic potentials, which were not all perfectly tuned for predicting the properties of both crystalline and amorphous phases. There is an opportunity for improvement here: incorporating a custom potential fitting procedure ahead of all the steps laid out in this project could improve the accuracy of the inter-atomic potentials used in the subsequent melt-quench simulations and computations of elastic properties. Ultimately, while simulations provided valuable qualitative insights, discrepancies with experimental data demonstrated the challenges of translating computational predictions into precise quantitative results.

Looking forward, improving the interatomic potentials used in simulations remains a critical step. Tailoring these potentials to accurately predict the mechanical properties of both crystalline and amorphous phases would greatly enhance the reliability and precision of molecular dynamics as a tool for designing metallic glass materials. Furthermore, investigating the glass-forming ability (GFA) of alloys is of great importance. Many of the metallic glasses analysed in this project are almost certainly impossible to form at realistic cooling rates, meaning that, while they might be the hardest in theory, they lack practical utility because they cannot be produced in practice. A deeper understanding of GFA could bridge this gap, ensuring that computational studies focus on alloys with real-world applicability. Finding ways to predict both GFA and mechanical properties would bring us closer to designing metallic glasses that are both theoretically exceptional and practically feasible.

This thesis explored the potential and limitations of molecular dynamics simulations for predicting the mechanical properties of metallic glasses. By focusing on the Al-Cu-Zr system, it has provided data and insights into the complex relationships between composition, structure, and elastic properties. While the findings may not break new ground, they add to the broader conversation in the field and demonstrate how computational tools can be applied in the pursuit of designing harder metallic glasses. This thesis represents an early step in understanding these fascinating materials and their potential applications. It reflects the culmination of much learning and effort, and I am sincerely grateful to my advisors, collaborators, and peers for their guidance and support. While much more remains to be explored, I hope the groundwork laid here proves to be a small but useful contribution for those who continue to study metallic glasses.

Acknowledgements

I would like to express my deepest gratitude to Dr. Emilia Olsson, my thesis supervisor, for her invaluable guidance, unwavering support, and remarkable patience throughout this journey. Her expertise and encouragement were instrumental in completing this work.

I am also deeply thankful to Jon, Barsha, and everyone else at ARCNL for their collaboration and support. Their assistance, particularly in helping me develop the extensive computer code required for this project, was invaluable. The programming effort was a significant and complex undertaking, and their contributions greatly enhanced the success of this work.

To my family and friends, thank you for your encouragement and unwavering belief in me. Your support has been a source of strength throughout this process.

Finally, I would like to thank the University of Amsterdam for providing the environment in which I pursued my master's degree, the people over at SURF for access to and support with the Snellius supercomputer, and NWO for their financial support during this research.

References

[1] Graeme Ackland, Adrian Sutton, and Vasek Vitek. Twenty five years of finnis–sinclair potentials. *Philosophical Magazine*, 89(34–36):3111–3116, December 2009.

[2] Patrick Avery, Xiaoyu Wang, Corey Oses, Eric Gossett, Davide M. Proserpio, Cormac Toher, Stefano Curtarolo, and Eva Zurek. Predicting superhard materials via a machine learning informed evolutionary structure search. *npj Computational Materials*, 5(1), September 2019.

[3] M. I. Baskes. Modified embedded-atom potentials for cubic materials and impurities. *Physical Review B*, 46(5):2727–2742, August 1992.

[4] Alexey Bolesta. Calculation of dynamic hardness by molecular dynamics. *EPJ Web of Conferences*, 221:01005, 2019.

[5] Werner Buckel. Elektronenbeugungs-aufnahmen von dünnen metallschichten bei tiefen temperaturen. *Zeitschrift für Physik*, 138(2):136–150, April 1954.

[6] Xing-Qiu Chen, Haiyang Niu, Dianzhong Li, and Yiyi Li. Modeling hardness of polycrystalline materials and bulk metallic glasses. *Intermetallics*, 19(9):1275–1281, September 2011.

[7] Y. Q. Cheng, E. Ma, and H. W. Sheng. Atomic level structure in multicomponent bulk metallic glass. *Physical Review Letters*, 102(24), June 2009.

[8] G. Clavier, N. Desbiens, E. Bourasseau, V. Lachet, N. Brusselle-Dupend, and B. Rousseau. Computation of elastic constants of solids using molecular simulation: comparison of constant volume and constant pressure ensemble methods. *Molecular Simulation*, 43(17):1413–1422, May 2017.

[9] Maarten de Jong, Wei Chen, Thomas Angsten, Anubhav Jain, Randy Notestine, Anthony Gamst, Marcel Sluiter, Chaitanya Krishna Ande, Sybrand van der Zwaag, Jose J Plata, Cormac Toher, Stefano Curtarolo, Gerbrand Ceder, Kristin A. Persson, and Mark Asta. Charting the complete elastic properties of inorganic crystalline compounds. *Scientific Data*, 2(1), March 2015.

[10] Jinglian Du, Bin Wen, Roderick Melnik, and Yoshiyuki Kawazoe. Phase stability, elastic and electronic properties of cu–zr binary system intermetallic compounds: A first-principles study. *Journal of Alloys and Compounds*, 588:96–102, March 2014.

[11] Gang Duan, Katrien De Blauwe, Mary Laura Lind, Joseph P. Schramm, and William L. Johnson. Compositional dependence of thermal, elastic, and mechanical properties in cu–zr–ag bulk metallic glasses. *Scripta Materialia*, 58(3):159–162, February 2008.

[12] Rahele Fereidonnejad, Ahmad Ostovari Moghaddam, and Mohammad Moaddeli. Modified embedded-atom method interatomic potentials for al-ti, al-ta, al-zr, al-nb and al-hf binary intermetallic systems. *Computational Materials Science*, 213:111685, October 2022.

[13] A. Figini Albisetti, C.A. Biffi, and A. Tuissi. Synthesis and structural analysis of cu10zr7. *Journal of Alloys and Compounds*, 544:42–45, December 2012.

[14] F. M. Gao and L. H. Gao. Microscopic models of hardness. *Journal of Superhard Materials*, 32(3):148–166, June 2010.

[15] A. Lindsay Greer. Metallic glasses. *Science*, 267(5206):1947–1953, March 1995.

[16] Olivier Hardouin Duparc. On the origins of the finnis–sinclair potentials. *Philosophical Magazine*, 89(34–36):3117–3131, December 2009.

[17] Vahid Hasannaeimi and Sundeep Mukherjee. Noble-metal based metallic glasses as highly catalytic materials for hydrogen oxidation reaction in fuel cells. *Scientific Reports*, 9(1), August 2019.

[18] Y. He, S. J. Poon, and G. J. Shiflet. Synthesis and properties of metallic glasses that contain aluminum. *Science*, 241(4873):1640–1642, September 1988.

[19] Anubhav Jain, Shyue Ping Ong, Geoffroy Hautier, Wei Chen, William Davidson Richards, Stephen Dacek, Shreyas Cholia, Dan Gunter, David Skinner, Gerbrand Ceder, and Kristin A. Persson. Commentary: The materials project: A materials genome approach to accelerating materials innovation. *APL Materials*, 1(1), July 2013.

[20] Jing Jiang, Zhen Lu, Jie Shen, Takeshi Wada, Hidemi Kato, and Mingwei Chen. Decoupling between calorimetric and dynamical glass transitions in high-entropy metallic glasses. *Nature Communications*, 12(1), June 2021.

[21] Young-Min Kim and Byeong-Joo Lee. A modified embedded-atom method interatomic potential for the cu–zr system. *Journal of Materials Research*, 23(4):1095–1104, April 2008.

[22] W. KLEMENT, R. H. WILLENS, and POL DUWEZ. Non-crystalline structure in solidified gold–silicon alloys. *Nature*, 187(4740):869–870, September 1960.

[23] Shinji Kobayashi, Koji Maeda, and Shin Takeuchi. Computer simulation of atomic srtucture of cu57zr43amorphous alloy. *Journal of the Physical Society of Japan*, 48(4):1147–1152, April 1980.

[24] Chunliu Li, Jia She, Mingjun Pang, Wenchao Yang, and Yongzhong Zhan. Phase equilibria in the al-zr-nd system at 773 k. *Journal of Phase Equilibria and Diffusion*, 32(1):24–29, November 2010.

[25] Ming-Xing Li, Yi-Tao Sun, Chao Wang, Li-Wei Hu, Sungwoo Sohn, Jan Schroers, Wei-Hua Wang, and Yan-Hui Liu. Data-driven discovery of a universal indicator for metallic glass forming ability. *Nature Materials*, 21(2):165–172, November 2021.

[26] H. Liebermann and C. Graham. Production of amorphous alloy ribbons and effects of apparatus parameters on ribbon dimensions. *IEEE Transactions on Magnetics*, 12(6):921–923, November 1976.

[27] Yu-Ching Lin, Yao-Chuan Tsai, Takahito Ono, Pan Liu, Masayoshi Esashi, Thomas Gessner, and Mingwei Chen. Metallic glass as a mechanical material for microscanners. *Advanced Functional Materials*, 25(35):5677–5682, August 2015.

[28] Dmitri V. Louzguine-Luzgin and Akihisa Inoue. *Bulk Metallic Glasses*, page 131–171. Elsevier, 2013.

[29] J. F. Lutsko. Generalized expressions for the calculation of elastic constants by computer simulation. *Journal of Applied Physics*, 65(8):2991–2997, April 1989.

[30] Avik Mahata, Tanmoy Mukhopadhyay, and Mohsen Asle Zaeem. Modified embedded-atom method interatomic potentials for al-cu, al-fe and al-ni binary alloys: From room temperature to melting point. *Computational Materials Science*, 201:110902, January 2022.

[31] N. Mattern, J. Bednarčik, S. Pauly, G. Wang, J. Das, and J. Eckert. Structural evolution of cu–zr metallic glasses under tension. *Acta Materialia*, 57(14):4133–4139, August 2009.

[32] M. I. Mendelev, Y. Sun, F. Zhang, C. Z. Wang, and K. M. Ho. Development of a semi-empirical potential suitable for molecular dynamics simulation of vitrification in cu-zr alloys. *The Journal of Chemical Physics*, 151(21), December 2019.

[33] M.I. Mendelev, M.J. Kramer, R.T. Ott, D.J. Sordelet, D. Yagodin, and P. Popel. Development of suitable interatomic potentials for simulation of liquid and amorphous cu–zr alloys. *Philosophical Magazine*, 89(11):967–987, April 2009.

[34] Omid Mokhtari, Min-Su Kim, Hiroshi Nishikawa, Fumiyoshi Kawashiro, Satoshi Itoh, Takehiko Maeda, Tetsuya Hirose, and Takaki Eto. Investigation of formation and growth behavior of cu/al intermetallic compounds during isothermal aging. *Transactions of The Japan Institute of Electronics Packaging*, 7(1):1–7, 2014.

[35] H. Okamoto. Cu-zr (copper-zirconium). *Journal of Phase Equilibria and Diffusion*, 33(5):417–418, July 2012.

[36] Hugo M. Ortner, Peter Ettmayer, and Hans Kolaska. The history of the technological progress of hardmetals. *International Journal of Refractory Metals and Hard Materials*, 44:148–159, May 2014.

[37] Kyoung-Won Park, Chang-Myeon Lee, Masato Wakeda, Yoji Shibutani, Michael L. Falk, and Jae-Chul Lee. Elastostatically induced structural disordering in amorphous alloys. *Acta Materialia*, 56(19):5440–5450, November 2008.

[38] S. Pauly, G. Liu, G. Wang, J. Das, K. B. Kim, U. Kühn, D. H. Kim, and J. Eckert. Modeling deformation behavior of cu–zr–al bulk metallic glass matrix composites. *Applied Physics Letters*, 95(10), September 2009.

[39] A. Peker and W. L. Johnson. A highly processable metallic glass: Zr41.2ti13.8cu12.5ni10.0be22.5. *Applied Physics Letters*, 63(17):2342–2344, October 1993.

[40] Suchismita Sarker, Robert Tang-Kong, Rachel Schoeppner, Logan Ward, Naila Al Hasan, Douglas G. Van Campen, Ichiro Takeuchi, Jason Hattrick-Simpers, Andriy Zakutayev, Corinne E. Packard, and Apurva Mehta. Discovering exceptionally hard and wear-resistant metallic glasses by combining machine-learning with high throughput experimentation. *Applied Physics Reviews*, 9(1), January 2022.

[41] Adit Sharma and Vladislav Zadorozhnyy. Review of the recent development in metallic glass and its composites. *Metals*, 11(12):1933, November 2021.

[42] Yong Shen and Jian Xu. Improving plasticity and toughness of cu-zr-y-al bulk metallic glasses via compositional tuning towards the cuzr. *Journal of Materials Research*, 25(2):375–382, February 2010.

[43] Chunguang Tang and Peter Harrowell. Anomalously slow crystal growth of the glass-forming alloy cuzr. *Nature Materials*, 12(6):507–511, April 2013.

[44] David M. Teter. Computational alchemy: The search for new superhard materials. *MRS Bulletin*, 23(1):22–27, January 1998.

[45] Yongjun Tian, Bo Xu, and Zhisheng Zhao. Microscopic theory of hardness and design of novel superhard crystals. *International Journal of Refractory Metals and Hard Materials*, 33:93–106, July 2012.

[46] Alessandro Troglia, Cyrian Leriche, Mike L. van de Poll, Christoph Morscher, Gert H. ten Brink, Bart J. Kooi, Bart Weber, and Roland Bliem. Bridging the gap between high-entropy alloys and metallic glasses: Control over disorder and mechanical properties of coatings. *Materials Today Communications*, 41:110604, December 2024.

[47] Hui Wang, Wojciech Dmowski, Yang Tong, Zengquan Wang, Yoshihiko Yokoyama, Jittisa Ketkaew, Jan Schroers, and Takeshi Egami. Nonaffine strains control ductility of metallic glasses. *Physical Review Letters*, 128(15), April 2022.

[48] Logan Ward, Dan Miracle, Wolfgang Windl, Oleg N. Senkov, and Katharine Flores. Structural evolution and kinetics in cu-zr metallic liquids from molecular dynamics simulations. *Physical Review B*, 88(13), October 2013.

[49] Peng Yu and H.Y. Bai. Poisson's ratio and plasticity in cuzral bulk metallic glasses. *Materials Science and Engineering: A*, 485(1–2):1–4, June 2008.

[50] Y. Zhang, N. Mattern, and J. Eckert. Atomic structure and transport properties of cu50zr45al5 metallic liquids and glasses: Molecular dynamics simulations. *Journal of Applied Physics*, 110(9), November 2011.

[51] Yongxing Zhao, Tikun Pang, Jiaxin He, Xiaoma Tao, Hongmei Chen, Yifang Ouyang, and Yong Du. Interdiffusion behaviors and mechanical properties of cu-zr system. *Calphad*, 61:92–97, June 2018.

[52] Va Şerban, C Codrean, D Uţu, and A Ercuţa. Fe-based bulk metallic glasses used for magnetic shielding. *Journal of Physics: Conference Series*, 144:012037, January 2009.

A Appendix

A.1 Elastic Moduli of the Al-Cu and Al-Zr Alloys

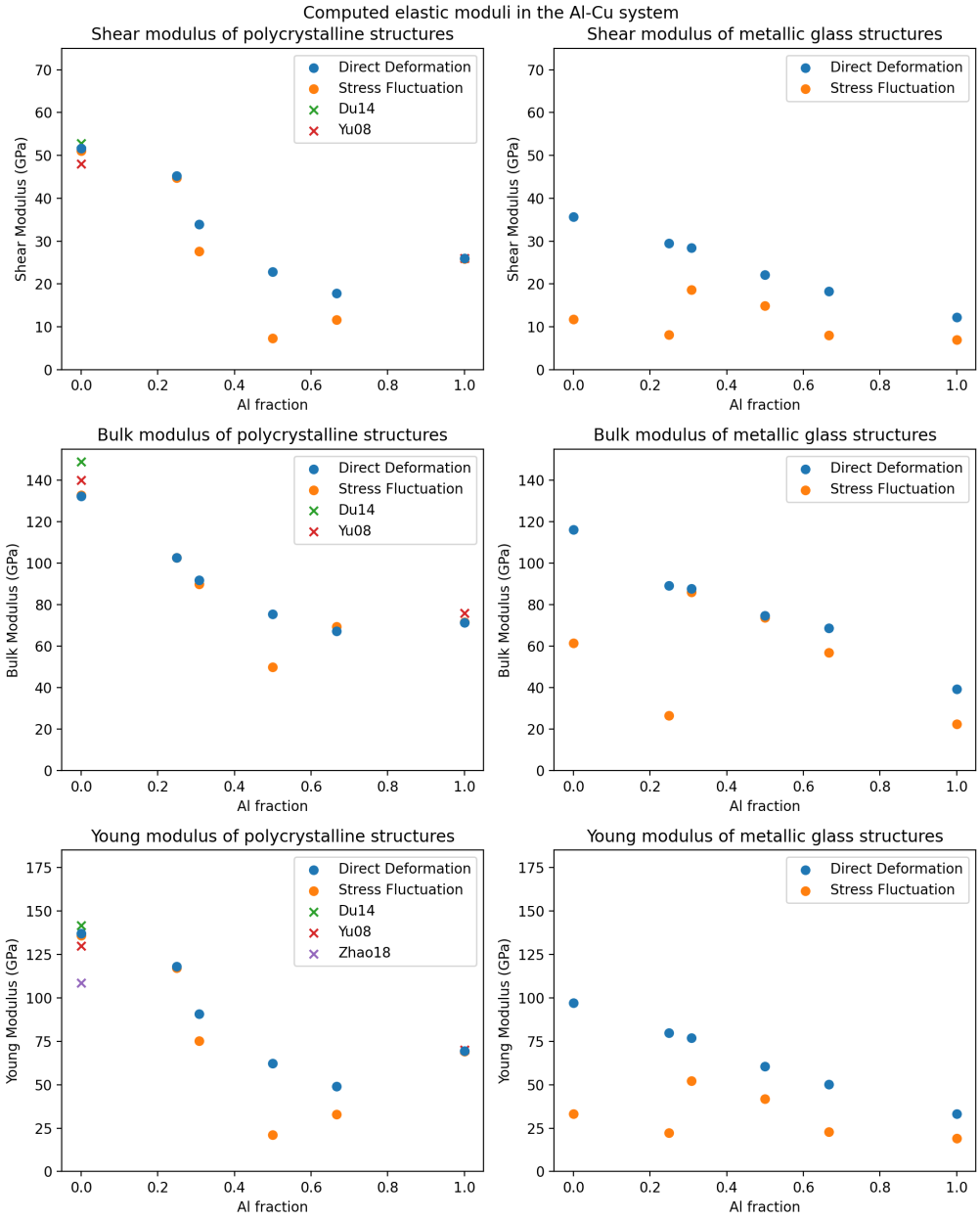

Figure 24: Bulk, shear, and Young's modulus in GPa of a number of alloys in the Al-Cu system, both in a polycrystalline and a metallic glass phase, plotted as a function of the percentage of aluminium atoms. Results obtained using the direct deformation method are shown in blue, and results obtained using the stress fluctuation method are shown in orange. The chemical formulae of the crystal structures are (from left to right) Cu, $AlCu_3$, Al_4Cu_9, $AlCu$, Al_2, and Al

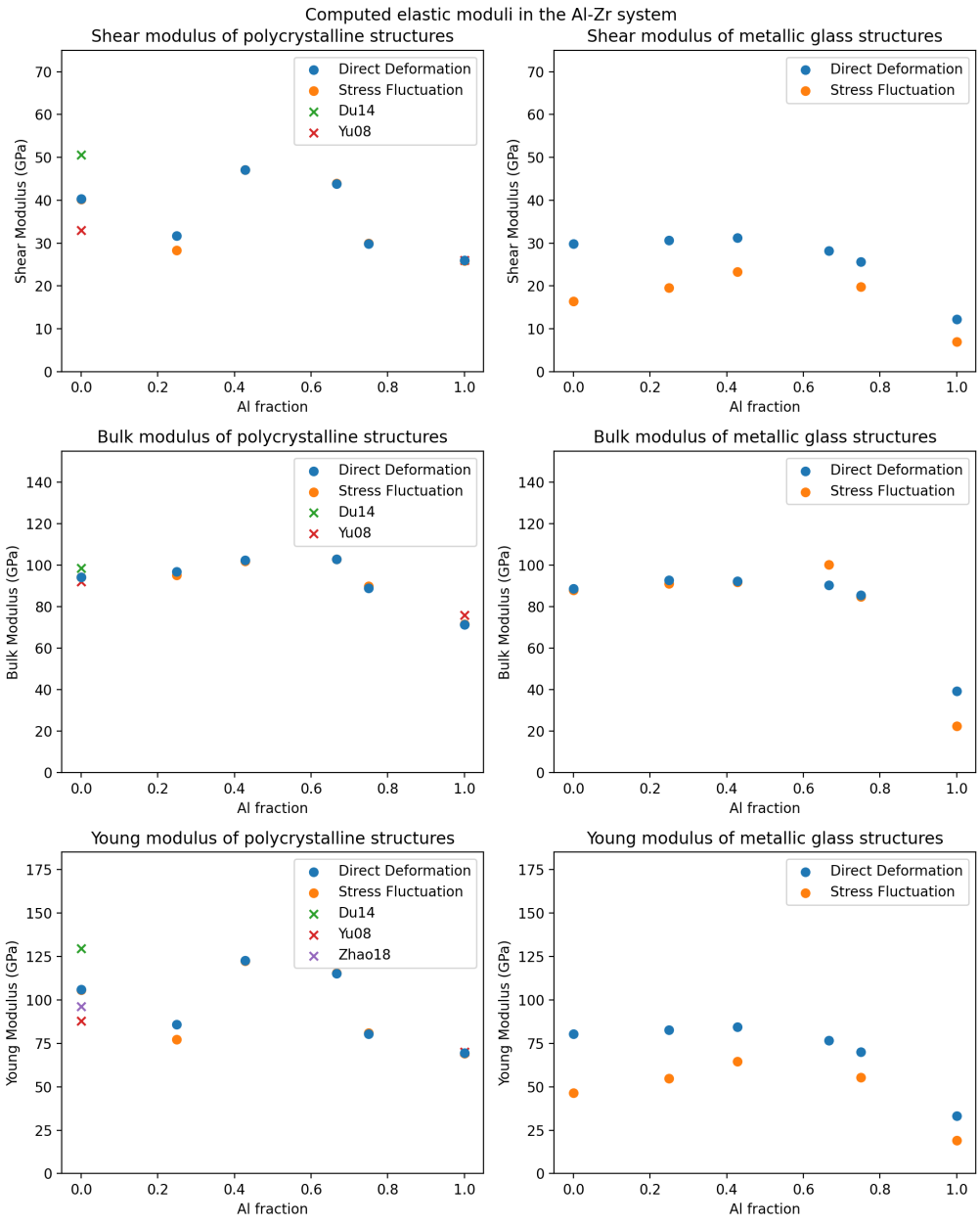

Figure 25: Bulk, shear, and Young's modulus in GPa of a number of alloys in the Al-Zr system, both in a polycrystalline and a metallic glass phase, plotted as a function of the percentage of aluminium atoms. Results obtained using the direct deformation method are shown in blue, and results obtained using the stress fluctuation method are shown in orange. The chemical formulae of the crystal structures are (from left to right) Zr, $AlZr_3$, Al_3Zr_4, Al_2Zr, Al_3Zr, and Al.

A.2 Binary Phase Diagrams

Figures 26, 27, and 28 show the phase diagrams of the Cu-Zr, Al-Cu, and Al-Zr binary systems respectively. Data retrieved from references [35, 34, 24].

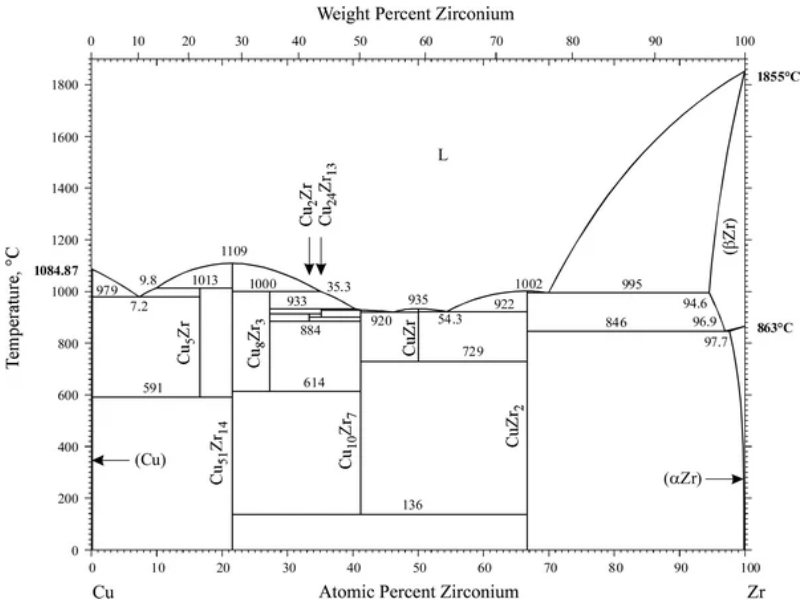

Figure 26: The Cu-Zr binary phase diagram [35].

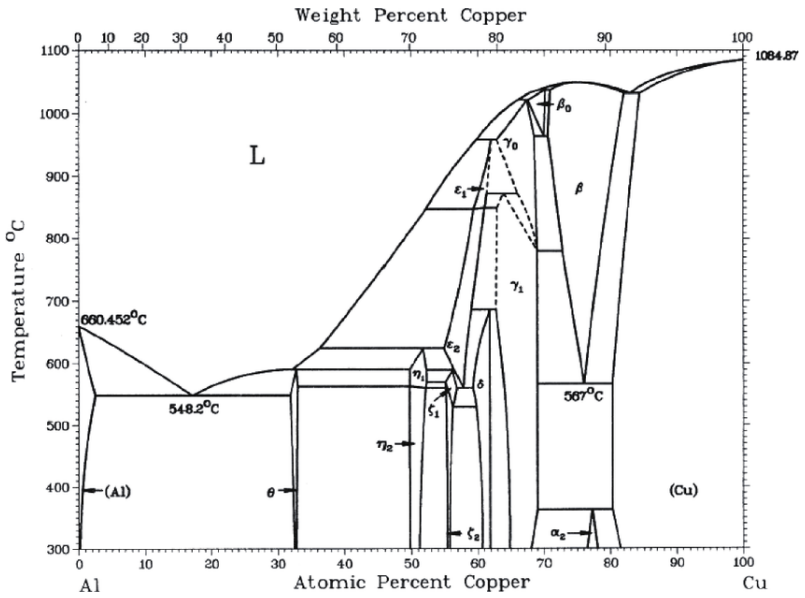

Figure 27: The Al-Cu binary phase diagram [34].

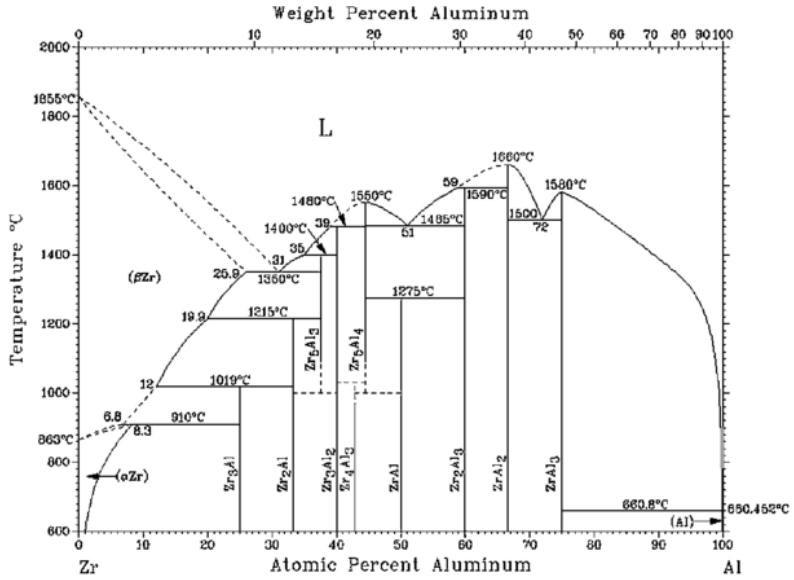

Figure 28: The Al-Zr binary phase diagram [24].

A.3 Interatomic Potential Parameters

This section lists the potential parameters for the Cu-Zr-Al MEAM potential used for the simulations in this project. The potential was developed by combining three binary MEAM potentials as outlined in section 3.2 [12, 30, 21]. The first two tables list the single element parameters. The first table contains the standard MEAM parameters [3] while the second table contains additional parameters required by LAMMPS for the MEAM library file. Additionally the contents of the LAMMPS MEAM parameter file is listed below the tables.

	alpha	b0	b1	b2	b3	t0	t1	t2	t3
Al	4.685597682	3.2	2.6	6	2.6	1	3.05	0.51	7.75
Cu	5.154830083	3.83	2.2	6	2.2	1	2.72	3.04	1.95
Zr	4.450190833	2.45	1	3	2	1	6.3	-3.3	-10

	lat	z	ielement	atwt	alat	esub	asub	rozero	ibar
Al	fcc	12	13	26.982	4.044650788	3.36	1.16	1	3
Cu	fcc	12	29	63.546	3.613315652	3.54	0.94	1	3
Zr	hcp	12	40	91.22	3.2	6.36	0.68	1	3

```
augt1 = 0.0
delr = 0.1
erose_form = 2.0
ialloy = 2.0
rc = 5.0

rho0(1) = 1.0
rho0(2) = 1.0
rho0(3) = 1.0

Ec(1,1) = 3.36
delta(1,2) = 0.2
Ec(1,3) = 5.511237
Ec(2,2) = 3.54
Ec(3,2) = 5.07
Ec(3,3) = 6.36

alpha(1,1) = 4.64779884
alpha(1,2) = 4.65
alpha(1,3) = 4.494343
alpha(2,2) = 5.17741504
alpha(3,2) = 4.78347011
alpha(3,3) = 4.45012373

re(1,1) = 2.86
re(1,2) = 2.53
re(1,3) = 2.892635
re(2,2) = 2.5575
re(3,2) = 2.8221
re(3,3) = 3.2

attrac(1,1) = 0.025
attrac(1,2) = 0.1
attrac(1,3) = 0.030009
attrac(2,2) = 0.025
attrac(3,2) = 0.025
attrac(3,3) = 0.0
```

```
repuls(1,1) = 0.025
repuls(1,2) = 0.1
repuls(1,3) = 2e-06
repuls(2,2) = 0.025
repuls(3,2) = 0.025
repuls(3,3) = 0.0

lattce(1,1) = 'fcc'
lattce(1,2) = 'b1'
lattce(1,3) = 'b2'
lattce(2,2) = 'fcc'
lattce(3,2) = 'b2'

nn2(1,1) = 1.0
nn2(1,2) = 1.0
nn2(1,3) = 1.0
nn2(2,2) = 1.0
nn2(3,2) = 1.0
nn2(3,3) = 1.0

zbl(1,1) = 0.0
zbl(1,3) = 0.0
zbl(2,2) = 0.0
zbl(3,2) = 0.0
zbl(3,3) = 0.0
```

```
Cmax(1,1,1) = 2.8
Cmax(1,1,2) = 2.8
Cmax(1,1,3) = 2.8
Cmax(1,2,1) = 2.8
Cmax(1,2,2) = 2.8
Cmax(1,3,1) = 2.8
Cmax(1,3,3) = 1.44
Cmax(2,1,2) = 2.8
Cmax(2,2,2) = 2.8
Cmax(2,2,3) = 1.44
Cmax(2,3,2) = 1.44
Cmax(2,3,3) = 2.8
Cmax(3,1,1) = 2.8
Cmax(3,1,3) = 1.44
Cmax(3,2,2) = 1.44
Cmax(3,2,3) = 2.8
Cmax(3,3,1) = 2.8
Cmax(3,3,2) = 1.44
Cmax(3,3,3) = 1.44

Cmin(1,1,1) = 0.49
Cmin(1,1,2) = 0.0
Cmin(1,1,3) = 0.680273
Cmin(1,2,1) = 0.5
Cmin(1,2,2) = 0.9
Cmin(1,3,1) = 0.3852
Cmin(1,3,3) = 1.092511
Cmin(2,1,2) = 1.0
Cmin(2,2,2) = 1.21
Cmin(2,2,3) = 1.21
Cmin(2,3,2) = 1.1025
Cmin(2,3,3) = 1.1025
Cmin(3,1,1) = 0.569374
Cmin(3,1,3) = 1.079323
Cmin(3,2,2) = 1.1025
Cmin(3,2,3) = 1.1025
Cmin(3,3,1) = 0.680084
Cmin(3,3,2) = 1.0
Cmin(3,3,3) = 1.0
```